SAR Remote Sensing of Canadian Coastal Waters using Total Variation Optimization Segmentation Approaches

by

Tae-Jung Kwon

A thesis
presented to the University of Waterloo
in fulfillment of the
thesis requirement for the degree of
Master of Science
in
Geography

Waterloo, Ontario, Canada, 2011

AUTHOR'S DECLARATION

I hereby declare that I am the sole author of this thesis. This is a true copy of the thesis, including any required final revisions, as accepted by my examiners.

I understand that my thesis may be made electronically available to the public.

Abstract

The synthetic aperture radar (SAR) onboard Earth observing satellites has been acknowledged as an integral tool for many applications in monitoring the marine environment. Some of these applications include regional sea-ice monitoring and detection of illegal or accidental oil discharges from ships. Nonetheless, a practicality of the usage of SAR images is greatly hindered by the presence of speckle noises. Such noise must be eliminated or reduced to be utilized in real-world applications to ensure the safety of the marine environment. Thus this thesis presents a novel two-phase total variation optimization segmentation approach to tackle such a challenging task. In the total variation optimization phase, the Rudin-Osher-Fatemi total variation model was modified and implemented iteratively to estimate the piecewise smooth state by minimizing the total variation constraints. In the finite mixture model classification phase, an expectation-maximization method was performed to estimate the final class likelihoods using a Gaussian mixture model. Then a maximum likelihood classification technique was utilized to obtain the final segmented result. For its evaluation, a synthetic image was used to test its effectiveness. Then it was further applied to two distinct real SAR images, X-band COSMO-SkyMed imagery containing verified oil-spills and C-band RADARSAT-2 imagery mainly containing two different sea-ice types to confirm its robustness. Furthermore, other well-established methods were compared with the proposed method to ensure its performance. With the advantage of a short processing time, the visual inspection and quantitative analysis including kappa coefficients and F1 scores of segmentation results confirm the superiority of the proposed method over other existing methods.

Acknowledgements

First of all, I am deeply grateful to my advisor, Professor Dr. Jonathan Li, for his continuous support, mentoring, encouragement, and friendship throughout my research. I am deeply impressed with his endless enthusiasm and thirst for academic research. Without his genuine guidance, I could have not accomplished the submission of two papers and the creation of this M.Sc. thesis.

I also want to express my heartfelt appreciations to my thesis committee member, Professor Dr. Richard Kelly, and the two thesis readers, Professor Dr. Claude Duguay and Dr. Su-Yin Tan for the valuable time they shared in providing helpful comments. I would also like to thank the graduate officer, Professor Dr. Richard Kelly, and the graduate studies administrative assistant, Ms. Lynn Finch at the Department of Geography and Environmental Management, University of Waterloo, for helping to provide additional teaching assistantships to reduce my financial burden.

Special thanks go to Dr. Xianfeng Zhang, Associate Professor at the Institute of Remote Sensing and GIS, Peking University, China and Canadian Ice Service, Environment Canada for providing COSMO-SkyMed and RADARSAT-2 SAR images, which were essential in completing this thesis.

Many thanks to Dr. Alexander Wong at the Department of Systems Design Engineering, University of Waterloo, for sharing his precious times and providing valuable office consultation sessions. The benefits I have received from him are purely immeasurable.

I also wish to thank many of my friends, especially Mark Steenhof, SungHoon Kim, Hamad Yousif, Tongil Kim, Yiyoung Choi, Ja-Ho Seo, YoungJae Kim, HoonSub Song, and Yuanming Shu for their encouragements and companionships in and outside of my school life.

Most of all, my deepest gratitude goes to my parents, JoongDal Kwon and ChulJae Jung; parents-in-law, MyungRae Lee and WanJin Jang; my beautiful elder sister, Hee-Jin Kwon, her husband, Eric Chow, and their lovely two kids, Justin and Aaron; my good-hearted second elder sister, Hee-Sun Kwon, and two brother-in-laws, HaeYoung Park and his wife KyungSook Lee, JaeMan Kim and his wife JungSook Lee for providing a tremendous wealth of unconditional love and sincere support.

Lastly, I would like to devote this thesis to my beautiful wife, YongBin Lee, for her greatest love and sacrifice in making this thesis possible, and my two adorable children, Chelsea Chae-Yeon and Brandon Hun-Yule, for making my life enjoyable and delightful.

Dedications

To My Greatest Parents, JoongDal Kwon and ChulJae Jung,

To the Love of My Life, YongBin Lee,

&

In Memory of My Mother-In-Law, WanJin Jang, 1939 - 2010

Table of Contents

List of Figures

List of Tables

Chapter 1

Introduction

This introduction addresses environmental issues of Canadian coastal waters. Section 1.1 presents two oceanographic case studies that emphasize the importance of oil-spill and sea-ice monitoring. In Section 1.2, the fundamental principle of synthetic aperture radar (SAR) imaging is described. The feasibility of using SAR to monitor coastal waters from Earth observing satellites as a proactive measure to prevent environmental damage is investigated in Section 1.3. In Section 1.4, the objectives and scope of the thesis are stated. Finally, the structure of the thesis is presented in Section 1.5.

1.1 Environmental Issues of Canadian Coastal Waters

Canada's coastal waters face many environmental threats, which in turn can have a serious impact on our health and well-being. Two of the key marine environmental issues, namely oil-spills as well as sea-ice changes in Canadian coastal waters and the Arctic, are discussed in-depth in Subsections 1.1.1 and 1.1.2 respectively.

1.1.1 Oil-spills in Canadian Coastal Waters

One of the most significant factors contributing to the degradation of the quality of the marine environment is either accidental or deliberate oil-spill (Topouzelis, 2008). Only about 10 % of oil-spills come from natural sources such as leakage from the bottom of the ocean (Kubat et al., 1998). Further, many oil-spills are deliberate, motivated by the desire to reduce dumping and filtering costs (Brekke & Solberg, 2005). Taking only the oil released by ships, it is estimated that 75% of oil spillage in the oceans comes from routine operations, including the transfer of oil, while only 25% derives from accidental spills (Grau & Groves, 1997; Indregard et al., 2005).

Oil-spills can have serious effects on the marine environment, and cause permanent ecological damage. Tiny species like plankton that lives in the upper layers of the ocean, are particularly at risk because they are very much exposed to floating oil-spills (Gin et al., 2001). However the consequences can be much worse. Because planktons that are at the bottom of the food chain will be eaten by various other small sea animals and species of fish, which then will accumulate oil and associated chemicals in their bodies. They themselves will eventually be eaten by bigger animals such as sea birds, seals and people. Consumption of polluted seafood and animals can consequently bring human health risks. Oil-spills can have large negative economic consequences on both the personal and national levels as well. The livelihood of people residing near coastal areas, particularly those who are solely depend on fishing and tourism can be heavily affected by oil-spills (NOAA, 2007).

The recent catastrophe that occurred on April 20, 2010 in the Gulf of Mexico is a severe example of the kinds of negative impacts, ranging from environmental to economic, that an oil-spill can cause. This catastrophic event was largely deemed as the worst environmental disaster in American history, with many casualties, excessive ecological damage and profound economic consequences. Reportedly the losses attributable by this incident cost approximately 22.6 billion USD, and this does not include environmental and economic losses that may yet be sustained over the long term. Nearly 7,000 animals including birds, turtles, dolphins and other mammals were killed (Park et al., 2010). Further, large numbers of fishermen lost their source of income, and their lives are now at risk. The tourism industry has also been heavily affected, with collateral damage even to neighbouring areas, where many tourists are now hesitant to travel even though they have yet to see a direct environmental impact.

Canada is very much exposed to the threat of oil-spills. Strikingly enough, about a dozen oil-spills occur on a daily basis in Canadian waters, and every year more than 300,000 seabirds are killed by oil in just the Atlantic waters alone (de Abreu et al., 2006). The greatest potential threat is to the East Coast of Canada where the volume of oil carried is staggering. In 2006, just in Placentia Bay Newfoundland, more than 1,000 vessels transported approximately 50 billion litres of crude oil (Suzuki, 2011). The west coast of Canada also faces the threat of oil-spills. British Columbia’s coast is internationally known for its luxuriant forests, abundant marine life and rich cultural heritage. Oil-spills in this region can potentially damage Canada’s global reputation as a world leader in environmentalism. Nonetheless, accidental oil-spill occur much too frequently in Canadian waters. In August

2006, the vessel M/V Westwood Anette suffered a fuel tank puncture and spilled approximately 29,000 litres of oil at Squamish terminal just north of Vancouver (see Figure 1.1). It cost $1 million to clean up heavily contaminated areas such as estuary marshes, and many Canada Geese were coated with oil (Ministry of Environment, 2006). Another incident occurred shortly after in July 2007 when a 24-inch crude oil pipeline was punctured, resulting in the spillage of approximately 234,000 litres of crude oil near the Barnett Highway in Vancouver (Ministry of Environment, 2007). Fifty residential properties were affected by this incident and a section of the Barnett highway was closed for several days, which caused expensive traffic delays. In addition, a 1,200 m long shoreline was affected. Due to the extent of the contamination, the cleanup work took nearly eleven months and officially ended in June 2008 (Ministry of Environment, 2007).

In light of the frequency of these accidental oil-spills, and in order to minimize the environmental and economic impacts, a continuous, effective and responsive strategy for monitoring the oceans is essential (Reed et al., 1999; Etkin, 2005).

Figure 1.1 Oil leaking from M/V Westwood Anette at Squamish Terminal (left) and cleanup crews on scene (right). (Ministry of Environment, 2006).

1.1.2 Sea-ice Changes in Canadian Coastal Waters

Sea-ice changes in Canadian coastal waters have been a major concern, hence regarded as highly important to study its potential environmental impact. Not only can the study of sea-ice changes be used for predicting future climate changes, but also for providing essential information on marine transportation. The extent of sea-ice in both the northern Arctic and the southern Antarctica are enormous that sea-ice in those regions plays a vital role in regulating the overall climate changes of the Earth (National Snow and Ice Data Center, 2011). Having acknowledged the importance of the study of sea-ice changes to foresee the potential consequences that may be incurred in near or far future, the need for monitoring such changes has been regarded as high priority.

Canada is largely affected by ice. In winter, there is over 4 million km^2 of Canadian waters that are covered by ice and more surprisingly, the amount of ice melted in this area during a period starting from November to end of August is sufficient to cover 60% of Canada's land (Environment Canada, 2011). Various forms of ice including sea-ice, lake ice, river ice and icebergs are affecting different aspects of Canadian's life in many ways including marine transportation, commercial fishing, tourism and recreation, local weather patterns and long-term climate (Environment Canada, 2011).

Recently, there has been an increased concern about global warming that has drawn Canadians' attention. The current trend of rising temperatures has been constantly warming the Arctic and directly affecting the enormous amount of ice present in Canadian waters

(Stirling & Parkinson, 2006). This trend will eventually lead to a bigger problem that can cause severe consequences to human life and Earth's natural environment. Global climate models (GCMs) indicated that the temperature over the Canadian Arctic would continue to increase, resulting in melting the sea-ice to a significant extent of causing a huge implication in many areas (Ford et al., 2008). In addition, the Fourth Assessment Report (AR4) of the United Nations Intergovernmental Panel on Climate Change (IPCC) indicated that the average Arctic temperatures have been increased by 0.74 ^{o}C in global average temperature in the past 100 years with sea level rise at a rate of 1.8 mm/year and 3.1 mm/year during the years 1961-2003 and 1993-2003, respectively (IPCC, 2007). Dramatic changes in temperature and sea level are shown in Figure 1.2.

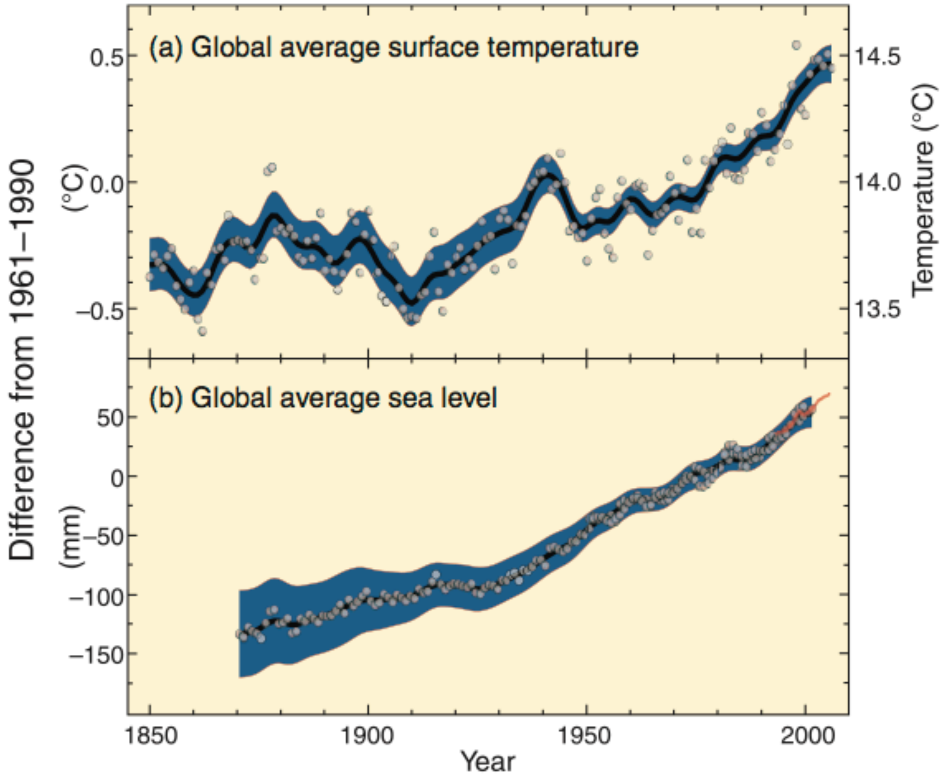

Figure 1.2 Changes in temperature and sea level (adapted from IPCC, 2007).

Thus, a continuous and proper sea-ice monitoring are emphasized in order to better understand the trend of rising temperature of the globe and plan for its potential impact.

A study of trend in climate change is not the sole reason for sea-ice monitoring since it could also be used as a primary source of information for determining optimal ship routes. The maritime activity in the ice concentrated regions, such as the eastern and northern waters of Canada, is greatly dependent on sea-ice as it controls the available navigable routes for safety reasons. In addition, routes through these regions can reduce the transportation costs (Natural Resources Canada, 2011). Figure 1.3 illustrates a vessel sailing over the Canadian Arctic ice-covered waters (Transport Canada, 2011). Stewart et al. (2007) showed that there had been an increased number of cruise ships visiting the Canadian Artic, and from 1984 to 2006 the number of ships visiting this region doubled to 22 ships (Buhasz, 2006). These facts indicate that the ocean environment has great potential in the world's tourism markets as it has been growing rapidly in the past years. Evidence that the Canadian Arctic will continue to observe increases in ship traffic is well supported by many sources in literature (Huebert, 2001; ACIA, 2004; Brigham & Ellis, 2004).

Thus, without a proper monitoring tool that detects the variability and condition of sea-ice, it will be almost impossible to come up with optimal ship routes that are safe, fast and cost-effective.

Figure 1.3 A vessel crossing over the Canadian Artic ice-covered waters (Transport Canada, 2011).

1.2 Fundamental Principle of SAR Imaging

SAR is a sidelooking radar system known to provide high spatial resolution (e.g. up to 1m in Spotlight mode of RADARSAT-2) covering a wide range of a target area (e.g. up to 500km^2 in ScanSAR Wide mode of RADARSAT-2). Furthermore, it is an active sensor that has the capability of recording objects at any time of the day under any weather condition (Aloisio & Cafaro, 2003). SAR onboard aircrafts or satellites emit electromagnetic radiation pulses that travel to the target area and get scattered off. The SAR antenna then records some of these backscattered pulses as amplitudes and phases, which then get preprocessed by the SAR-processor, producing an image (Cheny, 2002). A notable distinction between SAR and a typical radar system is the use of a synthetic antenna. A diagram is attached to better illustrate the basic principles of SAR in Figure 1.4. The notations, L_{SA}, R, V, λ, and Θ_A in

Figure 1.4 represent a synthetic aperture length (phased array), range, velocity, wavelength of emitted pulses, and aperture azimuth beamwidth, respectively and their relationships can be expressed as follows,

$$L_{SA} = \Theta_A R = \frac{\lambda R}{D_{AT}} \tag{1.1}$$

Actual size of the along-track antenna is expressed in a single dot (denoted as D_{AT}) that sums to form the synthetic aperture length. Range is determined by precisely measuring the total time took from the transmission to the receipt of the pulses by the antenna. Velocity is the speed of the platform carrying the SAR sensor. Also, the along track or alternatively called azimuth is another dimension that is perpendicular to range.

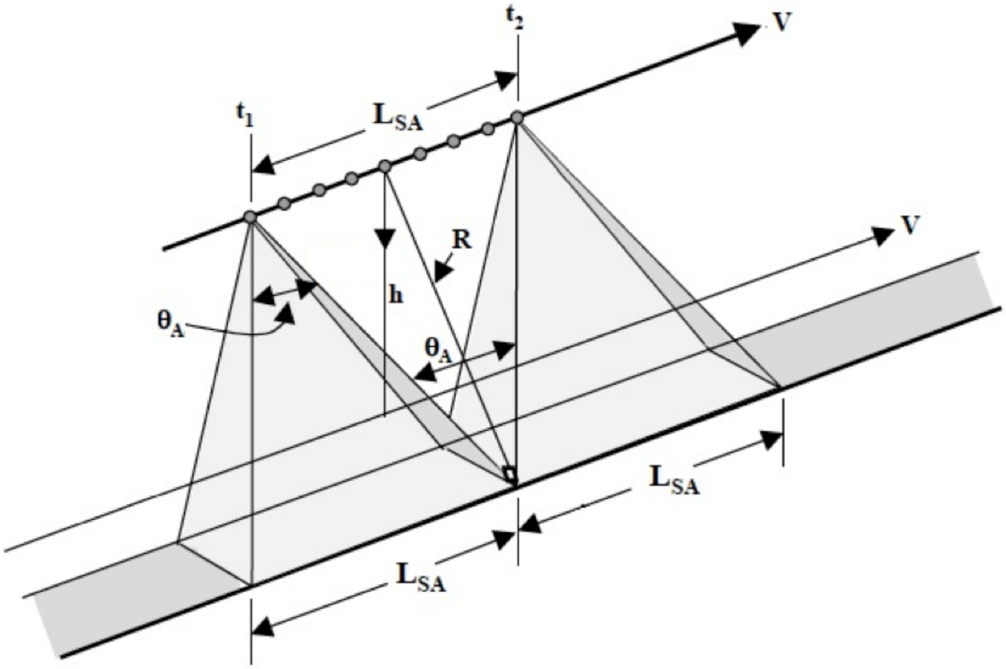

Figure 1.4 Basic Principles of Synthetic Aperture Radar (adapted from McCandless & Jackson, 2004).

A fundamental principle behind SAR is realized through utilization of an extremely large antenna or aperture, electronically. This means that SAR's physical antenna (represented as a small dot in the diagram) continuously records backscattered signals while traveling in the azimuth direction from t_1 (initial recording point) to t_2 (last recording point). The SAR-processor stores and processes all of these returned signals and reconstructs them as if they were recorded by the synthetic antenna whose length is equivalent to L_{SA}. In other words, as the platform moves along its trajectory, a synthetic aperture is generated by signal processing, which then creates the effect of elongating the actual SAR's small physical antenna (Wolff, 2011). By utilizing this unique technique, a higher resolution with a large swath width that maximizes the visibility and clarity of the subject target can be obtained.

1.3 Radar Imaging Satellites for Coastal Monitoring

As emphasized earlier, proper systems for monitoring marine environments to prevent the spreading of marine pollution caused by oil-spills, to determine the fastest and safest navigable ship routes, and to study and plan the global climate change are of high importance. Hence the key question now lies with choosing the optimal monitoring tool that is cost-effective and efficient.

There are many different tools for ocean and coastal monitoring including vessels, airplanes and satellites. Vessels may not be suitable for ocean and coastal monitoring since they cover limited area, however, they could be of good use when oil sampling is required

(Topouzelis, 2008). Alternatively, airplanes could be a good option since they cover a relatively large area although they are limited by the high costs. Thus, satellite surveillance has been favorably chosen over the other options due to its advantage of covering greater area at a relatively inexpensive cost. In the case of oil-spill monitoring, airborne surveillance may be of good help to identify the polluter, the extent and the types of oil-spills once the oil-spill is confirmed by the satellite sensors (Brekke & Solberg, 2005). Many claim that satellite surveillance, especially SAR, should be utilized as a first warning for the detection of oil-spills in the ocean and coastal waters as it could reduce the potential damage and response time of cleanup operations (Solberg et al., 1999; del Frate et al., 2000; Marghany, 2001). Even for sea-ice monitoring, a spaceborne remote sensing system is considered as the best candidate with similar underlying reasons given for oil-spill monitoring (Johannessen et al., 1997). Recent research that studied the feasibility of the application of radar in the marine environment states that the satellite surveillance, particularly the SAR, has become an integral tool for monitoring the overall coastal waters for pollution management and environmental protection (Helzel et al., 2010).

SAR is an active remote sensing system that operates in the microwave regions of the electromagnetic spectrum (EMS) and measures the return energy that has been either reflected or scattered back from the target surface. These reflected or scattered pulses are then captured by the receiving antenna and recorded to produce a two-dimensional (2-D) image. In coastal water monitoring, SAR is preferred over many other satellite sensors, including optical sensor, due to the following reasons:

(1) SAR is an active sensor that can provide its own source of illumination and therefore it can operate at any time of the day.

(2) SAR uses microwave electromagnetic radiation that can penetrate through rain, clouds and other atmospheric substances providing good monitoring capabilities.

(3) A SAR sensor is capable of monitoring a wide range of area (including inaccessible areas) at a very competitive cost compared to other ocean monitoring tools such as airborne ocean surveillance.

For more than three decades, satellite SAR data has been widely used for ocean and coastal environment monitoring. The various SAR sensors that are most suitable for ocean monitoring range from the Seasat launched in 1978 to the most recent Canadian RADARSAT-2, launched in 2007 are summarized in Table 1-1.

Table 1-1 Summary of Satellite SAR Sensors Suitable for Marine Environmental Monitoring. (extended from Gens, 2008)

Satellite	Agency	Operation	Frequency Band	Polarization	Swath width (km)	Repeat Cycle (days)	Best spatial resolution (m)
SEASAT	NASA	1978	L	HH	100	17	25
SIR-A	NASA	1981	L	HH	50	-	40
SIR-B	NASA	1984	L	HH	30	-	25
ERS-1	ESA	1991 to 2000	C	VV	100	3, 35, 336	30

JERS-1	JAXA	1992 to 1998	L	HH	75	44	18
SIR-C/X-SAR	NASA/DLR	1994 to 1994	C, L, X	Quad-pol	10-200	43	30
ERS-2	ESA	1995 to present	C	VV	100	35	30
RADARSAT-1	CSA	1995 to present	C	HH	50 - 500	24	8
SRTM	NASA/DLR	2000	C/X	Dual-pol	50-225	-	30
ENVISAT ASAR	ESA	2002 to present	C	Dual-pol	100 - 400	35	30
ALOS Palsar	JAXA	2006 to present	L	Quad-pol	70	46	10
TerraSAR-X	DLR	2007 to present	X	Dual-pol	10-100	11	1
COSMO-SkyMed	ASI	2007 to present	X	Quad-pol	10-200	16	1
RADARSAT-2	CSA/MDA	2007 to present	C	Quad-pol	25-500	24	1

NASA launched the first civilian satellite SAR sensor known as Seasat in 1978. This satellite was equipped with a L-band SAR operated at a single polarization mode (HH). Not too long after its first launch, NASA launched the Shuttle Imaging Radar, SIR-A in 1981 and SIR-B in 1984 whose data were extensively used to validate the wave-imaging model in the marine environment (Hasselmann et al., 1985). Then in 1991, the European Space Agency (ESA) launched the ERS-1 in 1991 and ERS-2 in 1995 specifically targeted for ocean monitoring. Many studies have been conducted based on the ERS-2 data, specifically in oil-spill and/or sea-ice monitoring and their feasibilities have been proven to be suitable (Gade & Alpers, 1999; Laxon et al., 2003; Brekke & Solberg, 2005). In the same year when ERS-2 was launched, the Canadian Space Agency (CSA) successfully launched RADARSAT-1, the first SAR sensor capable of providing various types of information at multiple beam modes with varying resolution. This was marked as one of a kind since it provides the compromise between resolution and wide coverage. The ScanSAR beam mode of RADARSAT-1 provides a good spatial resolution of 50-100 m with 300 – 500 km ground swath which is an ideal combination for monitoring a large ocean region. RADARSAT-1 was specifically designed to increase the monitoring capabilities in Canadian coastal waters and has been extensively used in various studies (Monaldo et al., 2001; de Miranda et al., 2004). In 2002, ESA launched the ENVISAT carrying 10 sophisticated optical and radar instruments on board to provide continuous monitoring of the Earth. Particularly, the ASAR (Advanced Synthetic Aperture Radar) onboard ENVISAT provides a data product at high spatial resolution up to 30 m covering a ground area of 110 km^2. In its wide swath and global monitoring mode, they both cover more than 400 km^2 at the resolution of 150 m and 1,000 m, respectively. With its enhanced monitoring advantages, it has been used specifically for oil-spill monitoring (Solberg et al., 2007; Zatyagalova et al., 2007; Brekke & Solberg, 2008). In 2007, the first X-band SAR satellites, German TerraSAR-X and Italian COSMO-SkyMed were flown into space ensuring the continuous observations of the Earth with enhanced capabilities. Usability of their data has been widely adopted for oil-spill monitoring (Trivero et al., 2007; Ciappa et al., 2009; Kim et al., 2010; Velotto et al., 2010). In the same year, CSA launched RADARSAT-2, a follow-on to RADARSAT-1. RADARSAT-2 was designed in a way that could provide powerful monitoring advancements including 1 m high spatial resolution in its Spotlight mode, flexibility in choosing different polarization modes for more precise observations. Its usability to real world applications has been emphasized in a wide range of areas such as environmental monitoring, ice mapping, disaster management and marine surveillance. Particularly, its application in marine surveillance accounting for oil-spill and sea-ice monitoring has been studied extensively (Flett et al., 2008; Wong et al., 2009; Bannerman et al., 2009; Tian et al., 2010; Eriksson et al., 2010).

Canada, as a leading country with possession of advanced RADARSAT-1 and -2 has begun a new mission development called the RADARSAT Constellation Mission (RCM) in 2005 and plans to launch three RCM satellites in 2014 and 2015. As shown in Figure 1.5, this program uses the three-satellite configuration that provides complete coverage of Canada's land and waters on a daily basis, and provides daily access to 95% of the world (Canadian Space Agency, 2011). Moreover, this program will deliver the enhanced monitoring capabilities such as maritime surveillance, disaster management and ecosystem monitoring.

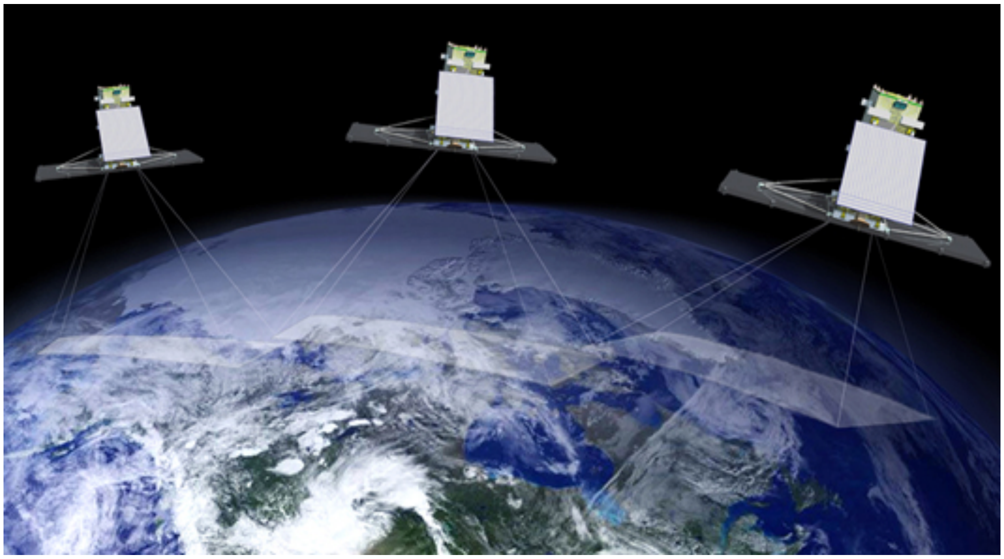

Figure 1.5 The RADARSAT Constellation Mission (Canadian Space Agency, 2011).

1.4 Thesis Objectives and Scope

Developing a fast, robust, and reliable segmentation method using SAR imagery for ocean monitoring applications is challenging. Moreover, developing a detection algorithm, which detects both oil-spill and sea-ice, is an even more intricate task. Thus, the main objective of this thesis is to develop a full and comprehensive automated feature detection algorithm that can be utilized not only in the aforementioned applications but also in other various applications involving SAR imagery. In this thesis, such challenges are reviewed and tackled thoroughly by incorporating the novel automated segmentation method called total variation optimization segmentation approach (TVOS) to better reflect the task of SAR intensity image segmentation. Due to the limited time given for data collections and associated testing, this thesis investigates the feasibility of the proposed method on dark-spot detection for oil-spill monitoring, and on two types of sea-ice and seawater detection for sea-ice monitoring. This method was tested using both synthetic and real-world SAR images whose information was recorded using single frequency and single polarization mode from COSMO-SkyMed (used for detecting dark-spots) and RADARSAT-2 (used for detecting sea-ice types). The objectives of the thesis are further explained by the following:

(1) Studying and understanding the complexity of the feature detection method using SAR intensity imagery.

(2) Developing and constructing a comprehensive segmentation framework that can be implemented in two different applications: (a) dark-spot detection for oil-spill monitoring, and (b) multiple sea-ice detection.

(3) Performing a quantitative analysis to confirm the superiority of the developed framework compared to other conventional approaches.

1.5 Thesis Structures

The rest of this thesis is organized as follows:

Chapter 2 introduces the feature detection in coastal waters, particularly focusing on the automated oil-spill detection and sea-ice detection using SAR imagery. This chapter also details the proposed total variation optimization segmentation approach using SAR intensity image.

Chapter 3 contains the first manuscript submitted to *ISPRS Journal of Photogrammetry and Remote Sensing*, entitled “Detecting Dark-spots in SAR Oil-Spill Imagery using a Total Variation Optimization Segmentation Approach”.

Chapter 4 includes the second manuscript submitted to *IEEE Transactions on Geoscience and Remote Sensing*, entitled “ETVOS: An Enhanced Total Variation Optimization Segmentation Approach for SAR Sea-ice Image Segmentation”.

Chapter 5 gives the conclusions including the summary of the findings of two submitted manuscripts, and investigates the recommended future work.

Chapter 2

Methodology for Detecting Features in SAR Imagery of Coastal Waters

Having acknowledged the importance of monitoring the coastal environment, the key question now arises of how to detect desired features in the seawaters using SAR intensity imagery.

In this chapter, the background of the feature recognition with regards to oil-spill detection and sea-ice detection with an emphasis on implementation of automated technique is delivered in Sections 2.1 and 2.2, respectively. In Section 2.3, a common problem that exists in a typical SAR image is further discussed. Section 2.4 details the proposed total variation optimization segmentation approach.

2.1 Automated Detection of Oil-spills in SAR Imagery

The mechanism built for detecting oil-spills in SAR imagery is based on the fact that oil films floating on the ocean reduce the amount of backscattering of the sea surface resulting in the formation of dark regions on SAR intensity imagery (Alpers & Huhnerfuss, 1989). The sea surface roughness plays a significant role since ocean phenomena, including oil-spills, can never be detected without varying sea surface roughness that is created by wind-generated short gravity-capillary waves. This indicates that the visibility of ocean phenomena is greatly affected by the speed of wind. It is commonly understood that the wind speed ranging from 3-10 m/s produces the best visibility of oil-spills (Brekke & Solberg, 2005). Having acknowledged this backscattering property, challenges arise that other man-made or natural phenomena, so called look-alikes, could possibly cause reduction in the backscattering signal similar to that caused by oil-spills on SAR intensity imagery thus making it very difficult to discriminate between oil-spills and look-alikes. Examples of look-alikes causing this include low wind areas, organic films, rain cells, current shear zones, grease ice, and eddies (Topouzelis, 2008).

There has been an increasing amount of SAR images received at analysis centres around the world for manual analyzing to verify if there are oil-spills in the received images (Brekke & Solberg, 2005). This implies a growing workload given to the operators who have to undertake extensive training to adapt manual oil-spills detection techniques. Decisions made by these operators can often be subjective (Indgregard et al., 2004). It is also very time consuming to analyze each dataset individually, thus, the importance of an automated oil-spills detection method that provides fast and reliable results is of high demand (Nirchio et al., 2005; Karathanassi et al., 2006; Solberg et al., 2007; Karantzalos & Argialas, 2008). A framework of detection algorithm of oil-spills using SAR imagery can be accomplished through three distinct steps as shown in Figure 2.1.

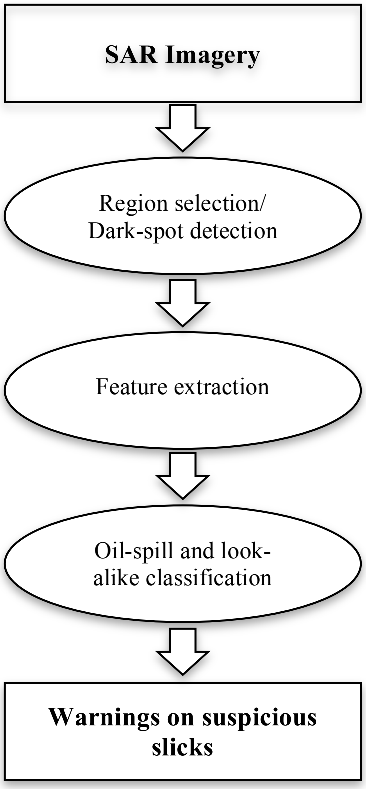

Figure 2.1 A common framework for detecting oil-spill (adapted from Brekke & Solberg, 2005).

The SAR image is input in the first step called region selection/dark-spot detection step. In this step, only dark-spots that contain actual oil-spills and other natural phenomena known as look-alikes are extracted while others are disregarded. Detected dark-spots are then processed in the second step where various features are extracted by analyzing the geometry and shape of the detected dark-spots. In addition, the differences in the physical characteristics of the backscattered signals of the dark-spot and neighbouring areas are further investigated (Brekke & Solberg, 2005). With the aid of the extracted features, oil-spills and look-alikes are classified in the final step to determine the presence of potential oil-spills and decide whether to send the aircraft to verify and/or to take relevant action.

The preliminary task, which is to detect dark-spots, has been regarded as the most critical and fundamental step since if no dark-spots are detected, then the real oil-spills can never be found in the later steps. Another important aspect of dark-spot detection is that a low degree of accuracy of detected dark-spots can negatively affect the feature extraction as well as the classification phase where an accurate discrimination between oil-spills and look-alikes are greatly hindered. Since manual detection is laborious and time consuming, a primary goal is to develop a fast, reliable, and robust automated dark-spot detection algorithm that can accurately extract dark-spots from the background so that the adverse effect in a later stage can be minimized and the likelihood of discriminating the actual oil-spills can be maximized.

2.2 Automated Detection of Sea-ice in SAR Imagery

Sea-ice detection using SAR imagery can be complicated as there are almost 30 different terms used to distinguish individual ice types and their conditions. Nonetheless, SAR has been regarded as the most important remote sensing instrument due to the advanced characteristics of SAR sensors as emphasized earlier. The mechanism of how SAR sensors collect backscattering response, specifically targeting in detection of sea-ice, varies as a function of various factors including frequency, polarization mode, angle of incidence, and the scattering characteristics of the target area. Moreover, season is another factor that plays a critical role in determining the ice types and conditions. Figures 2.2 and 2.3 illustrate how the aforementioned factors affect the strength of backscatter return signals.

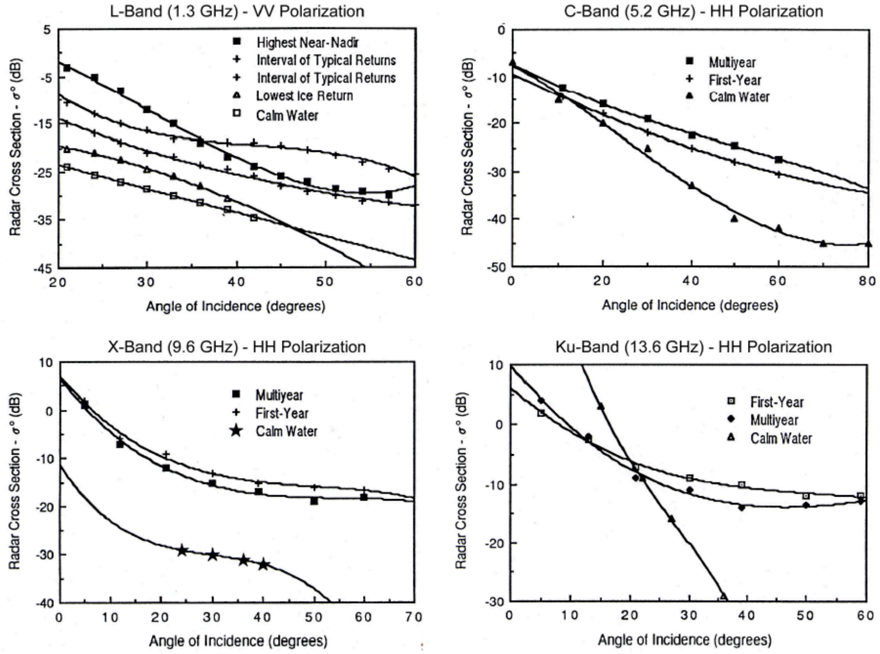

Figure 2.2 Radar backscatter cross sections at different frequency levels during summer (adapted from Onstott, 1992).

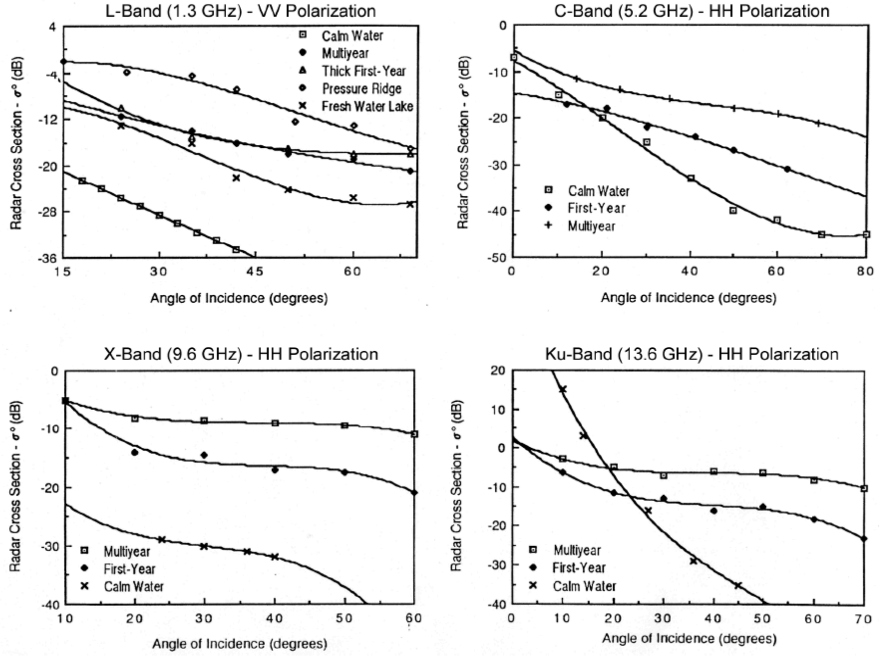

Figure 2.3 Radar backscatter cross sections at different frequency levels during winter (adapted from Onstott, 1992).

Two key surface parameters that affect the characteristics of the backscattering of sea-ice are surface roughness and the dielectric constant of sea-ice or open water (Onstott & Shuchman, 2004). The degree of surface roughness governs the amount of the reflected backscattering energy. This implies that the amount of backscattering energy return changes with respect to the surface roughness and thus, by analyzing the luminosity of returned energy, it can be determined whether first-year ice, multiyear ice, or open water is present. Figure 2.4 shows the backscatter interactions for three distinct features in the ocean.

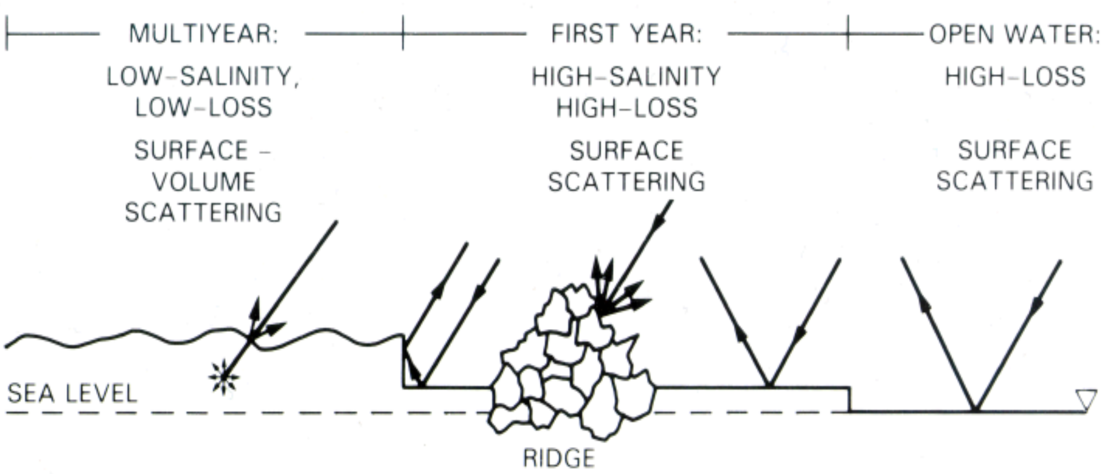

Figure 2.4 Backscatter interactions for multiyear ice, first year ice and smooth open water (adapted from Onstott, 1992).

The dielectric constant of sea-ice decreases as the degree of salinity decreases. The dielectric constant plays a critical role in determination of different types of sea-ice and other features in SAR intensity imagery. The dielectric constant is calculated by determining how much electromagnetic field is absorbed, dissipated, or reflected by natural substances or materials. The relationships between the dielectric constant and the strength of backscattering signals was determined by Deng & Clausi (2005) who stated that a material having a low dielectric constant (low salinity) reflects a high portion of SAR signals and would subsequently create a bright region in SAR intensity images. Multiyear ice having a lower salinity enables microwave electromagnetic pulses emitted by SAR to penetrate deeper, hence the gas bubbles and voids within the ice trigger a severe volume scattering that contributes to the large amount of backscattering recorded by SAR antennas (Onstott & Shuchman, 2004). Since the salinity of very thick sea-ice is near zero, it can be inferred that thicker sea-ice will tend to be brighter in colour (Deng & Clausi, 2005). On the contrary, new or fresh sea-ice tends to be darker in the image since they have a higher dielectric constant, as a result the amount of backscattering is low. As for the smooth open water, the backscattering will be near zero because of its surface smoothness and high salinity constant (Onstott & Shuchman, 2004). Thus, knowing how various sea-ice types appear in SAR imagery, different sea-ice types can be distinguished from each other.

Currently, an abundant amount of SAR sea-ice images are received and processed by trained sea-ice analysts at the Canadian Ice Service (CIS) on a daily basis. With these analyzed sea-ice images, maps are produced for sea-ice concentrated region monitoring. Unfortunately, all of the ice maps are still being generated by a manual digitization technique since the computer-assisted or automated segmentation method is not sufficiently robust and effective to ease the manual workloads at the CIS (Deng & Clausi, 2005). Therefore, the need for an automated segmentation technique using SAR imagery is of high importance as it will significantly reduce the cost and minimize the adverse effects caused by subjective/ biased interpretations made by sea-ice analysts (Clausi, 2001).

2.3 Common Challenge of Feature Detection from SAR Imagery

A common problem, yet the most fundamental and challenging task when using SAR imagery, is to eliminate speckle noise. Every SAR image contains vast amounts of multiplicative noise known as speckle. Speckle is caused mainly by constructive and destructive interference of reflective energy from a target surface as shown in Figure 2.5 (Richards & Jia, 2006). Because the transmitted and received SAR signals will not always be in-phase even in the homogenous target surface, the speckles may appear as slightly brighter or darker than the mean value.

Having speckle noise is a huge problem that limits visibility of features and leads to misinterpretation when analyzing SAR imagery. Having recognized the importance of eliminating speckle noise, many efforts have been put forth to develop a robust algorithm to effectively suppress speckle noise without changing the detailed feature characteristics within the image (Lee, 1980; Frost et al., 1982; Kuan et al., 1987; Yu & Acton, 2002; Achim et al., 2003; Marques et al., 2004). Among those, Lee, Frost and Kuan's adaptive filters are commonly used to despeckle SAR imagery prior to performing feature classification. Lee's adaptive filter, for instance, takes both spatial and intensity differences of pixels into account and can be effective in eliminating noise. However, because it calculates the average intensity rather than the individual intensity differences correlated to each pixel value within the local processing window, it may not be very robust when dealing with highly speckled images. Since SAR images always carry speckle noise, it remains a challenging task to develop a robust and efficient despeckling method to obtain desirable segmentation results.

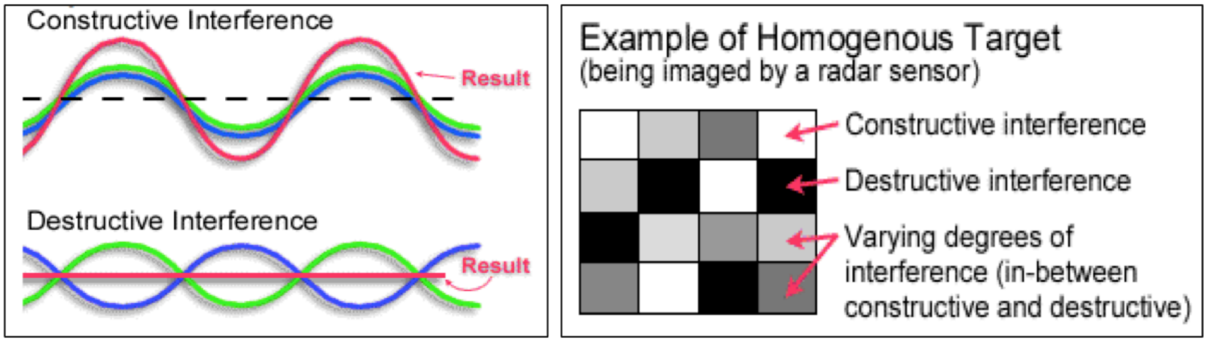

Figure 2.5 Description of speckle noises (adapted from Natural Resources Canada, 2005).

2.4 The Proposed Methodology

The proposed method is called total variation optimization segmentation (TVOS) and is motivated by the aforementioned challenging criteria that arises when dealing with SAR imagery to better handle the task of SAR image segmentation. The proposed TVOS algorithm is developed in a way that can satisfy a typical SAR image containing high speckle noise. To tackle this challenging task more efficiently, a two-phase algorithm is implemented. The overall flowchart of this method is provided in Figure 2.6.

The first phase uses a modified total variation optimization scheme, as described in Subsection 2.4.1, while the second phase utilizes a finite mixture model classification scheme, as described in Subsection 2.4.2.

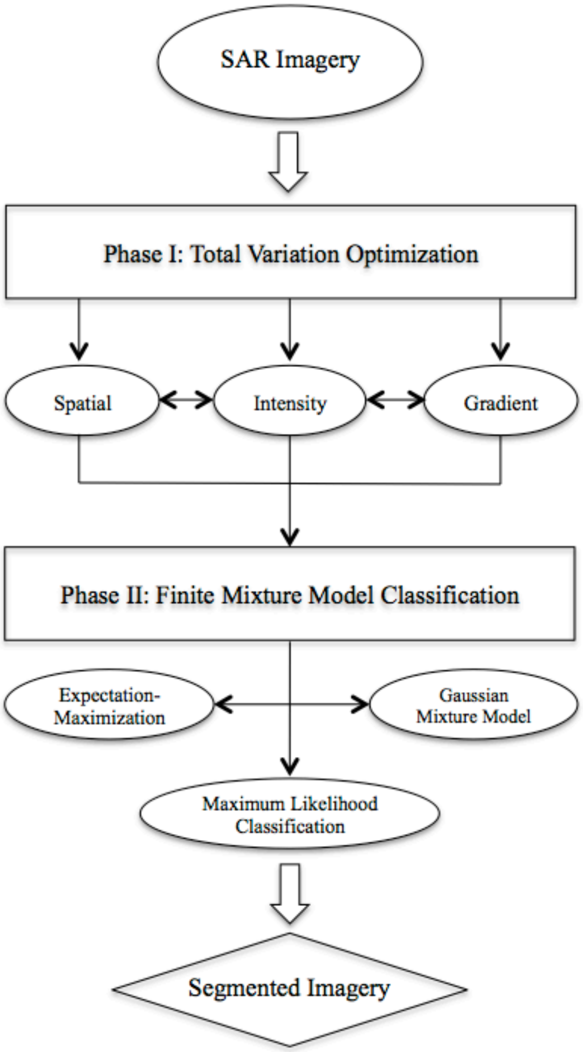

Figure 2.6 Flowchart of the proposed TVOS method.

2.4.1 Phase I: Total Variation Optimization

The presence of multiplicative speckle noise and many other artifacts in SAR imagery greatly hinders the process of obtaining a desirable segmentation result. An example of a typical SAR image, which will be used as a test image, is illustrated in Figure 2.7 and a graphical representation of speckle noise is illustrated in Figure 2.8. Note that this test image has been extracted from RADARSAT-1 oil-spill imagery covering the East Coast of Canada taken on July 10, 2007.

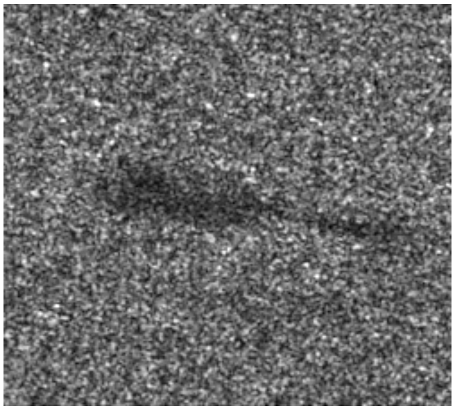

Figure 2.7 Test Image: A test SAR image containing a dark-spot in the centre with image size of 250 x 250 pixels.

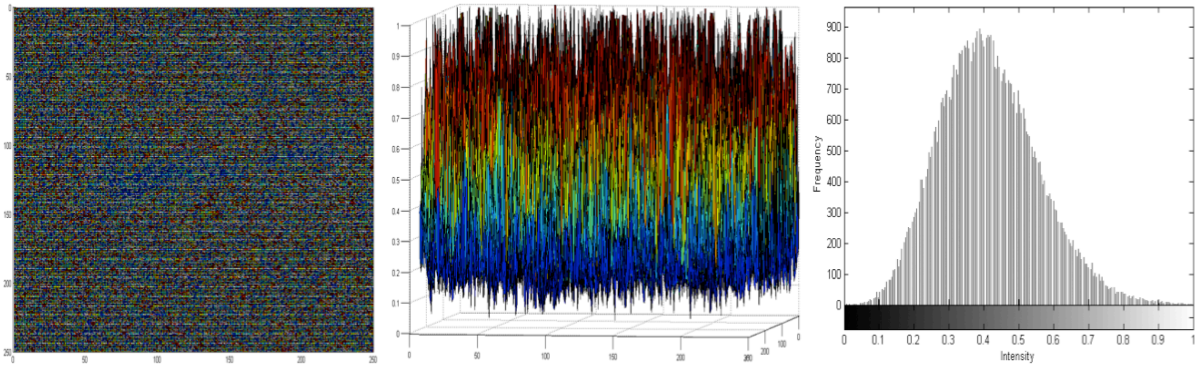

(a) (b) (c)

Figure 2.8 Graphical representation of speckle noise of the test image in (a) 2-D, (b) 3-D, and (c) histogram generated using the test image.

As can be seen from Figure 2.8(a), coherent speckles negatively affect the quality of the original SAR image such that the dark-spot can hardly be recognized by visual inspection.

The 3D pictorial representation, as shown in Figure 2.8(b), also illustrates the adversely affected SAR image due to speckle noise and other imaging conditions. It can be observed that the image intensity values fluctuate in a wide range from near 0 to 1 without posing any recognizable pattern for a subject target being dark-spot located at the centre of the test image. In addition, the histogram generated using the test image as shown in Figure 2.8(c) shows the unimodal pixel distribution indicating that two classes, the dark-spot and the background, are not properly recognized due to the presence of the speckle noise. With this highly speckled SAR image, good segmentation results are almost impossible to achieve.

In its simplest term, speckle noise can be treated by taking either spatial or intensity differences into account. When only considering the spatial differences between the neighbouring pixels and the centre pixel in that neighbourhood, it is assumed that pixel values in the images change slowly over time, and therefore it becomes appropriate to average them together. It is believed that taking the spatial characteristics would effectively eliminate the noise since they are less correlated than the actual signal values and hence it eliminates the noise while preserving the actual signal. However, the assumption that the pixel values vary slowly over time fails when the edge of an object in the image is reached. It is evident to state that the pixel values would be largely different around the edge so that making such an assumption is very dangerous. The question then arises of how to prevent the averaging across the edges while continuing to average in a smooth region where pixel values do slowly change over time. To overcome such challenges, the intensity difference is incorporated. The assumption made previously is ignored and the averaging of pixel values that have similar intensity values is enforced. Therefore pixels that have similar intensity values will be averaged. Previous research indicates that taking a gradient difference of pixels will also improve its edge preservation ability since pixels with large gradient differences are less likely to belong to the same region. As such, the first phase of the proposed TVOS method was inspired by the observations made when combining three difference terms, spatial, intensity, and gradient differences into account so that noise can be reduced in a highly speckled image while effectively preserving edges by incorporating a nonlinear combination of neighbouring pixel values.

Having acknowledged the importance of the aforementioned three difference terms, an optimization problem can be formulated to efficiently handle a SAR segmentation task. Let g be the observed SAR imagery, f be the piecewise smooth state of the observed g, and u be the residual state containing random noise. Their relationships can be expressed as follows,

$$g = f + u \tag{2.1}$$

One approach to solve this inverse problem can be realized by utilizing the Rudin-Osher-Fatemi Total Variation (ROFTV) model. Given the additive relationship in equation (2.1), the problem of image segmentation can be formulated into the minimization problem based on the existing ROFTV model (Rudin et al., 1992) shown by

$$\hat{f} = \operatorname{argmin}_f \left[\alpha \int_{\Omega} |f - g|^2 \, d\underline{x} + \beta \int_{\Omega} |\nabla f| \, d\underline{x} \right] \tag{2.2}$$

where Ω is an open set representing the image domain, and ∇f represents the finite intensity difference between neighboring pixels. The first term of equation (2.2) is the data fidelity term, while the second term is the total variation term that penalizes pixel intensity differences within regions to enforce piece-wise smoothness in *f*. In the ROFTV model, the goal is to progressively evolve a noisy SAR imagery, *g,* whose imaging condition is in non-piecewise smooth state containing non-separable classes into a piecewise smooth state, *f*. In the process of the evolution to achieve *f*, the total variation is minimized and the classes become well delineated.

As discussed earlier, incorporation of the intensity difference penalty term alone may not be sufficient, especially when the image is highly contaminated with speckle noises. As such, the existing ROFTV model has been modified by adding two additional total variation penalty terms; the spatial difference term, ∇x, and the gradient difference term, ∇k, to effectively and efficiently handle the SAR segmentation task. These additional total variation constraints will work simultaneously to enforce a piecewise smooth state of the image, in which the edges or boundaries of subject targets are preserved by the intensity and gradient difference terms while noise is treated by the spatial difference term. By observing the data histogram it was found that the statistical distribution of pixels in the SAR imagery generally followed a Gaussian distribution. Therefore, the proposed total variation penalty terms will be modeled with Gaussian functions. The first incorporated penalty term that enforces spatial difference between pixels can be expressed as follows (Tomasi & Manduchi, 1998),

$$x(\xi,\psi) = e^{-\frac{1}{2}\left(\frac{d(\xi,\psi)^2}{\sigma_x^2}\right)} \tag{2.3}$$

where

$$d(\xi,\psi) = d(\xi-\psi) = \left\|\xi-\psi\right\| \tag{2.4}$$

is the Euclidean distance between the centre pixel ψ, and the neighbouring pixel, ξ. x(ξ,ψ) measures the spatial closeness between pixels so that homogeneity of surrounding pixels is enforced. σ_x is the standard deviation for pixel difference and as its value gets larger, images will get smoother, in other words, it will blur more. This also implies that when a larger σ_x is used, pixels that are located further away from the centre pixel, ψ, are combined. This is mainly due to the fact that spatially nearby pixels are forced to merge together unless there is a pixel that has a large intensity difference when compared to the surrounding pixels.

The second penalty term that enforces the intensity difference between pixels can be expressed as follows (Tomasi & Manduchi, 1998),

$$f(\xi,\psi) = e^{-\frac{1}{2}\left(\frac{\left(\delta\left(s(\xi)\right),s(\psi)\right)^2}{\sigma_f^2}\right)} \tag{2.5}$$

where

$$\delta(\phi,s) = \delta(\phi - s) = \left\|\phi - s\right\| \tag{2.6}$$

is a measure of the distance between two intensity values ϕ at the neighbouring pixel ξ, and *s* at the centre pixel ψ. When computing the intensity difference between pixels, a smaller intensity difference will cause pixels to be merged together whereas pixels with large intensity differences will stay unchanged depending on the weight given by σ_f. Thus, pixels with the value of σ_f being closer to each other than σ_f are averaged, while pixels that are further from each other than the value σ_f are disregarded.

The last penalty term that enforces the gradient difference between pixels can be expressed as follows,

$$k\left(\xi,\psi\right)=e^{-\frac{1}{2}\left(\frac{\left(\tau\left(s\left(\xi\right)\right),s\left(\psi\right)\right)}{\sigma_k^2}\right)} \tag{2.7}$$

where

$$\tau\left(\omega,s\right)=\tau\left(\omega-s\right)=\left\|\omega-s\right\| \tag{2.8}$$

is a measure of the distance between two gradient difference values, ω, at the neighbouring pixel ξ, and *s* at the centre pixel, ψ. σ_k denotes the standard deviation of the gradient difference between pixels. Similar to the mechanism built for computing an intensity difference, the gradient difference is enforced between pixels since large gradient differences will have a small likelihood of belonging to the same class.

With these total variation constraints, the final formulation of the segmentation problem based on the modified ROFTV model can be rewritten as,

$$\hat{f}=\operatorname{argmin}_f\left[\alpha\int_\Omega\left|f-g\right|^2 d\underline{x}+\beta\int_\Omega\left(\left|\nabla f\right|+\left|\nabla x\right|+\left|\nabla k\right|\right)d\underline{x}\right] \tag{2.9}$$

As can be seen in equation (2.9), the additional total variation constraints, ∇*x* enforcing the spatial difference and ∇*k* enforcing the gradient difference, have been incorporated to extend the ROFTV model to better estimate the piecewise smooth state. To solve this problem in an efficient manner, an iterative weighted optimization strategy is utilized to approximate *f*, where the updated estimate, f_t at iteration *t* can be expressed by

$$\hat{f}_t = Z\int_{\Omega} \exp\left[\beta\left(|\nabla f| + |\nabla x| + |\nabla k|\right)\right]\hat{f}_{t-1}\, d\underline{x} \qquad (2.10)$$

where Z is a normalization term to ensure that the values do not go beyond the allowed range, and β is the regularization constant that helps to quickly reach the piecewise smooth state of the original noisy image.

To better explain what the first phase of the TVOS actually does, 2-D and 3-D graphical representations of the first phase treated test image at one iteration are given in Figure 2.9.

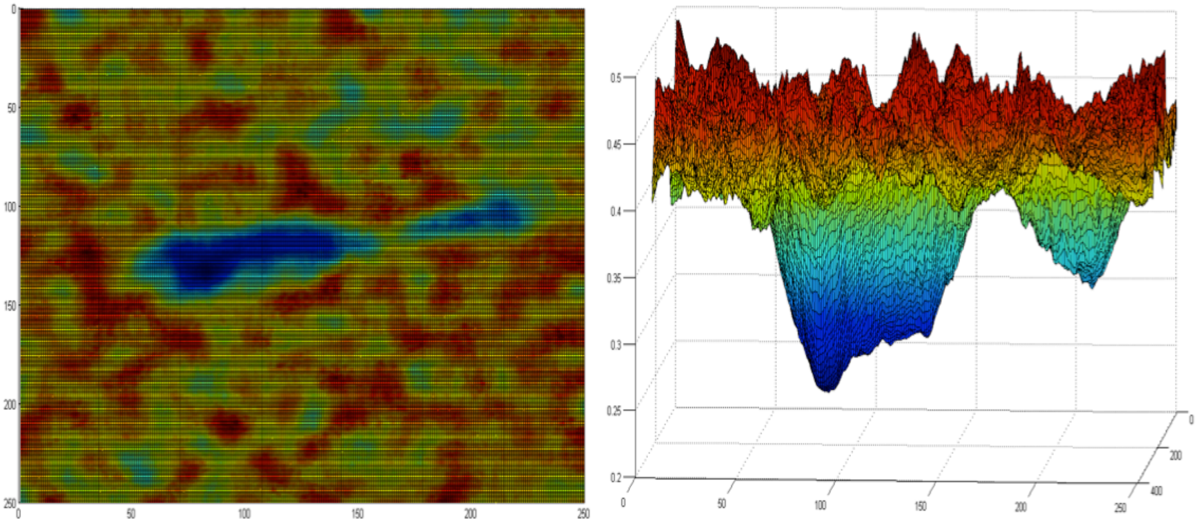

(a) (b)

Figure 2.9 Graphical representation of (a) 2-D, and (b) 3-D of the test image after being processed with total optimization phase at the 1st iteration.

As can be observed in Figure 2.9, the subject target in the original SAR image is now clearly recognizable (see Figure 2.9(a)). Also the 3-D graphical representation of the first-phase treated image shows two downward peaks, reflecting the original image correctly. This observation indicates that the coherent imaging noise has been significantly reduced when compared to the original test image and its untreated statistical distribution shown in Figure 2.8.

Another experiment was conducted where two iterations of total variation optimization phase were implemented as shown in Figure 2.10. It can be seen that speckle noise has been reduced again when compared to the results shown in Figure 2.9 and the number of extreme peaks have been significantly reduced (see Figure 2.10(b)). This clearly indicates that the image has come one step closer to a piecewise smooth state.

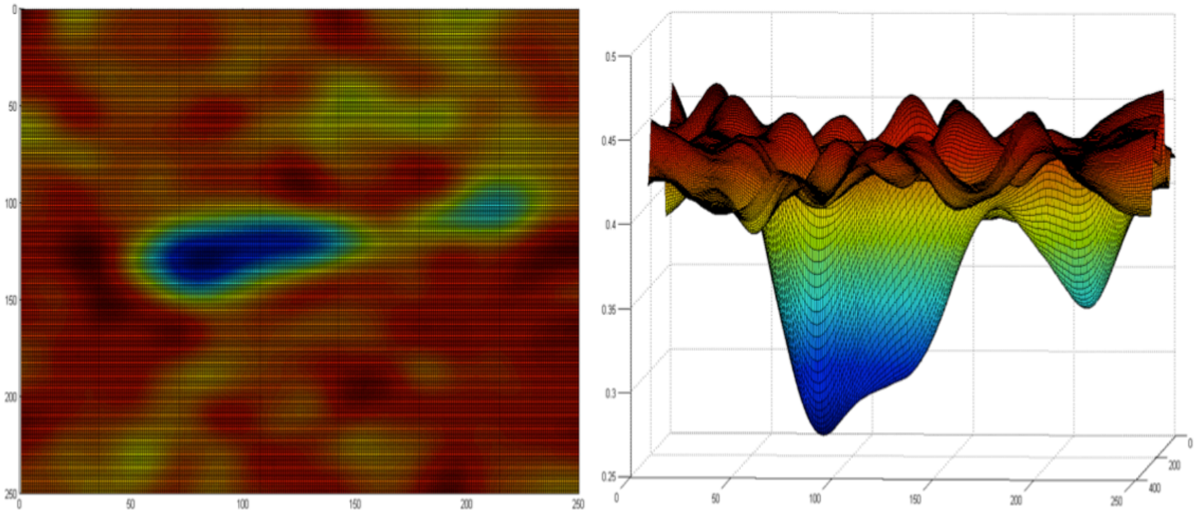

(a) (b)

Figure 2.10 Graphical representation of (a) 2-D, and (b) 3-D of Figure 2.5 after being processed with total optimization phase at the 2nd iteration.

From a theoretical perspective, running the total variation optimization phase iteratively would slowly evolve to a convergence in which the complete piecewise smooth state is realized. However, achieving such a steady state can be very expensive when considering the computational time (e.g. more than one hour), thus it is not well suited for practical purposes. Through the course of numerous tests, it was discovered that even running the optimization strategy for a limited number of iterations (one or two) produces a good approximation of the piecewise smooth state of the original noisy image where classes are easily separable, as clearly illustrated in Figures 2.9 and 2.10. Motivated by this observation, a faster finite mixture model classification strategy is utilized in the second phase of the proposed TVOS algorithm to approximate the final segmented result by efficiently enforcing the complete piecewise smoothness of the observed SAR intensity imagery.

2.4.2 Phase II: Finite Mixture Model Classification

In the second phase of the proposed TVOS method, a finite mixture model classification strategy was employed on what was achieved in the first phase to obtain the final segmentation result. First, a Gaussian mixture model (GMM) was utilized to estimate the unknown parameters in an effort to obtain a promising segmentation result using SAR intensity imagery.

Let n be the number of components within a Gaussian mixture model and let l be a class label where $l \in \{1, ..., n\}$. Furthermore, the set of unknown parameters to be estimated using a Gaussian mixture model is denoted as Θ,

$$\Theta = \left\{\mu_1,...,\mu_n,\sigma_1,...,\sigma_n,P\left(f=1\right),...P\left(f=n\right)\right\} \tag{2.11}$$

where μ, σ, and P(f) denote the mean at the centre of each Gaussian distributed parabola, standard deviation, and prior probability of an observed sub-class component within the mixture model, respectively. The goal is to precisely model the underlying distribution. With such a model, the probability of observing, $\hat{f}$ can be expressed by

$$p\left(\hat{f}\middle|\Theta\right) = \sum_{i}^{n} p\left(\hat{f}, l = i \middle|\Theta\right) \tag{2.12}$$

The next step is to compute the maximum likelihood estimates of the unknown parameters that maximize the probability of obtaining the observed data, $\hat{f}$. However, determination of unknown parameters is often intractable to solve analytically.

In order to solve this problem in more efficient manner, an expectation maximization (EM) technique is utilized. EM is a very popular method for finding the maximum likelihood estimates (MLE) of the unknown parameters and is used in various applications involving SAR imagery (Wang et al., 2005; Khan et al., 2007). EM consists of two steps that run in an iterative fashion until changes in the estimated parameters become marginal. The first step is called expectation (E) step where the log-likelihood function to predict the associated parameters in the mixture model is calculated as shown in the following equation (Piater, 2002).

$$E = \frac{p\left(\hat{f}_j\middle|\Theta_i\right)P(i)}{\sum_{u=1}^{n} p\left(\hat{f}_j\middle|\Theta_u\right)P(u)} \tag{2.13}$$

where each new data point $\hat{f}$ is generated by component i at the current estimates of Θ_i and P(i). After the associated parameters in Θ are estimated, a subsequent step called maximization (M) is entered. In this step, it attempts to find estimated parameters that maximize the expected log-likelihood function by updating the associated parameters that were initially determined in the previous E step. This is achieved by utilizing the following equation,

$$M = \sum_{j=1}^{v} \log p\left(\hat{f} \middle| \Theta\right) \tag{2.14}$$

The log-likelihood function is used since the logarithm is a function that increases monotonically, hence when the logarithm of a function reaches its highest or maximum value, the function itself reaches the same maximum point (McLachlan & Krishnan, 1997). Furthermore, since calculating the maximum of a function typically involves the computation of a derivative, it is much easier to deal with the maximized function as a log-likelihood function. Thus, the combined expectation-maximization scheme to estimate a set of unknown parameters, Θ at an updated value at *t* can be realized by (Dempster et al., 1977),

$$\Theta_{t+1} = \operatorname{argmax}_{\Theta} \sum_{j=1}^{v} \sum_{i=1}^{n} p\left(l_j = i \middle| \hat{f}_j, \Theta_t\right) \ln p\left(l_j = i \middle| \hat{f}_j, \Theta\right) \tag{2.15}$$

where,

$$p\left(l_j = i \middle| \hat{f}_j, \Theta_t\right) = \frac{p\left(\hat{f}_j \middle| l_j = i, \Theta_t\right) P\left(l_j = i \middle| \Theta_t\right)}{\sum_{u=1}^{n} p\left(\hat{f}_j \middle| l_j = u, \Theta_t\right) P\left(l_j = u \middle| \Theta_t\right)} \tag{2.16}$$

Finally, once unknown parameters are determined using EM, the maximum likelihood (ML) estimate of the final class l_f (target area or non-target area) at pixel $\underline{x}$ can be obtained by calculating the following,

$$\hat{l}\left(\underline{x}\right) = \arg\max_{l} p\left(\hat{f}\left(\underline{x}\right) \middle| l\right) \tag{2.17}$$

The final segmentation result achieved in the finite mixture model classification phase followed by the total variation optimization phase is illustrated in Figure 2.11. Dark-spots have been outlined in white contour lines to increase the visibility of results where only dark-spots have been detected. It is important to emphasize that such a result was obtained using the 1^{st} iterated product from the first total variation optimization phase.

As observed in Figure 2.11(a), the segmentation result clearly shows the subject target being detected in the test image. Also 3-D graphical representation as shown in Figure 2.11(b) describes the complete piecewise smoothness indicating that other imaging noises and artifacts have been completely removed, and only the subject target has been remained. Another notable achievement is a very short processing time that the segmentation result was obtained in approximately 5 seconds. Thus, it can be concluded that the proposed comprehensive segmentation approach is fast, robust, and effective in handling the complicated SAR segmentation task.

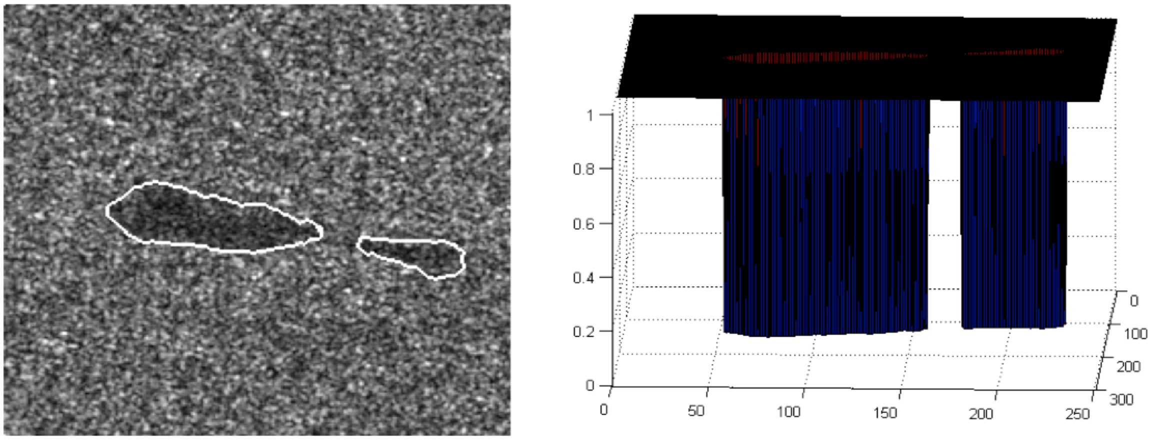

(a) (b)

Figure 2.11 (a) Final segmentation result of the test image achieved in a finite mixture model classification phase, and (b) 3-D representation of the segmentation result.

Chapter 3

Detecting Dark-spots in SAR Oil-spills Imagery using a Total Variation Optimization Segmentation Approach

Overview

The use of synthetic aperture radar (SAR) has been a vital part of dark-spot detection, a fundamental step leading ultimately to oil-spill monitoring and detection to protect our marine environment. However, it is often regarded as challenging, since there are numerous underlying imaging conditions such as inherent speckle noise that hinders a pleasing segmentation result. Thus, this paper presents a novel approach called total variation optimization segmentation (TVOS) to effectively extract dark-spots (possible oil slicks) in a timely manner. In the first part of this two-phase approach, a modified Rudin-Osher-Fatemi total variation model was employed iteratively to optimize and estimate the piecewise smooth state of the original noisy image by minimizing the total variation constraints. In the second phase, an expectation maximization approach was utilized to estimate the final class likelihoods by incorporating the Gaussian mixture model. Then, the final class containing possible oil slicks was obtained using the maximum likelihood classification method. The proposed method was examined on an artificial image at multiple noise levels and 46 subsets of the Italian COSMO-SkyMed X-band SAR imagery containing verified oil slicks. Moreover, the segmentation results were compared with other well-established methods to provide more effective comparisons. The visual and the quantitative kappa analysis demonstrated that the proposed method is fast, efficient, and robust in dark-spot detection.

3.1 Introduction

There are many different types of marine pollutants and one of the most significant threats contributing to the degradation of our marine environment and costal ecosystem is deliberate or accidental oil-spills discharged from transporting ships (Topouzelis, 2008). Reports have shown that a great portion of oil pollution also originates from routine ship activities such as tank washing and discharges from engine effluent that flow directly to the ocean (Lean & Hinrichen, 1999). Not only can oil pollution in coastal waters bring adverse effects on overall marine life and permanent environmental damage, but it can also result in environmental resources being wasted that will consequently lead to severe economic repercussions. In addition, the number of reported seabirds that have mistakenly landed on the oil-coated surface of the ocean annually and died is countless. Moreover, the livelihoods of many residents living near coastal areas are negatively affected as the majority of them wholly depend on fishing and tourism for their living (Jha et al., 2008). Recently in 2010, a catastrophic event involving an oil rig explosion in the Gulf of Mexico well illustrates the huge environmental and economical impact of oil-spills. The losses attributed by this incident are approximately 22.6 billion USD, not including the potential losses that will likely arise in the future. In addition, nearly 7,000 ocean animals including turtles, seals, and other mammals became victims of this disaster. Furthermore, many fishermen completely lost their source of income and the tourism industry has also been severely affected as people became hesitant to travel to the neighboring contaminated areas. Thus, the use of state-of-the-art technology such as synthetic aperture radar (SAR) has been recognized by many researchers for its potential in aiding oil-spills monitoring and detection due to its profound abilities of acquiring data covering large areas. In addition, SAR is effective since it can be used at any time of the day without being interrupted by rain, clouds, and other atmospheric substances (Nirchio et al., 2005; de Abreu et al., 2006; Keramitsoglou et al., 2006;).

Detection of oil-spills in SAR imagery is based on the fact that oil films in the ocean have a dampening effect on the short gravity-capillary waves, which reduce the backscattering being recorded by the SAR antenna. As a result, a dark region is formed having a high contrast difference compared to other surroundings (Migliaccio et al., 2005; Topouzelis, 2008). Since the quality of data greatly depends on the aforementioned waves, it is commonly said that the wind speed ranging from 3-10 m/s produces the best luminosity of oil-spills (Brekke & Solberg, 2005). Having mentioned the backscattering characteristics, one of the main challenges is to discriminate oil-spills from other man-made or natural phenomena such as algae, grease ice, rain cells, upwelling zones, current shear zones, low wind speed areas, and internal waves known as look-alikes (Girard-Ardlhuin et al., 2005; Topouzelis et al., 2007).

There have been many different approaches, ranging from manual to fully automated segmentation methods, developed so far to locate oil slicks in the ocean. As for manual oil-spill detection, there is a highly successful framework implemented by the Canadian Ice Service (CIS) called Integrated Satellite Tracking of Pollution (ISTOP) in operation since November 2006. This program primarily uses Canadian RADARSAT-1 C-band ScanSAR narrow beam mode images to extract the oil slicks. This system has minimized the workload of oil-spill analysts by providing them a geospatial workplace. In this workplace, they can review and overlay SAR images and other environmental information such as wind speed on the outputs derived from the Ocean Monitoring Workstation (OMW) developed by Satlantic Ltd (de Abreu et al., 2006). The OMW was developed for maritime surveillance, specifically targeting oil-spill monitoring and vessel detection using SAR images whose results are promising (Vachon et al., 2000). However, the judgment of analysts of whether the suspicious features are oil or non-oil regions can be very subjective and give varying confidence levels (Indregard et al., 2005). Moreover in ISTOP, the processing of nearly 5,000 SAR images that need to be verified by human analysts each year is very laborious and time consuming. Thus, the development of an efficient and effective computer detection algorithm that can help prioritize ocean pollution warnings is essential.

Generally speaking, oil-spill detection using SAR imagery can be accomplished through three distinct steps; (1) dark-spot detection which identifies all dark-spots presented in a SAR image as candidates of potential oil sills, 2) feature extraction from the dark-spot candidates, and (3) classification of dark-spots to distinguish between oil-spills and look-alikes (Brekke & Solberg, 2005). In this paper, we are primarily targeting the dark-spot detection step. This step is the most critical and fundamental step of all because if no potential dark-spots containing actual oil-spills are found in this step, they can never be discovered in a later stage. One of the major challenging tasks to tackle in the dark-spot detection step is to reduce or eliminate the inherent multiplicative noise, called speckle, caused by constructive and destructive interferences of the reflective energy from the target surface (Richards & Jia, 2006). Also, there is likely a contrast variation between dark regions and the seawater background depending on environmental characteristics such as local sea state, oil-spill types, or physical characteristics of the SAR sensor such as resolution and incident angle (Karathanassi et al., 2006). This difficulty is illustrated in Figure 3.1 in which the statistical distribution of pixel values forms a unimodal shaped curve indicating that there is no intensity difference between the dark region and background. This is not true as there is a clear visual distinction. This phenomenon occurs mainly due to the presence of speckle noises. Thus, an effective and efficient method to eliminate speckle noise without changing the original structure of the SAR image for an optimal classification result is essential.

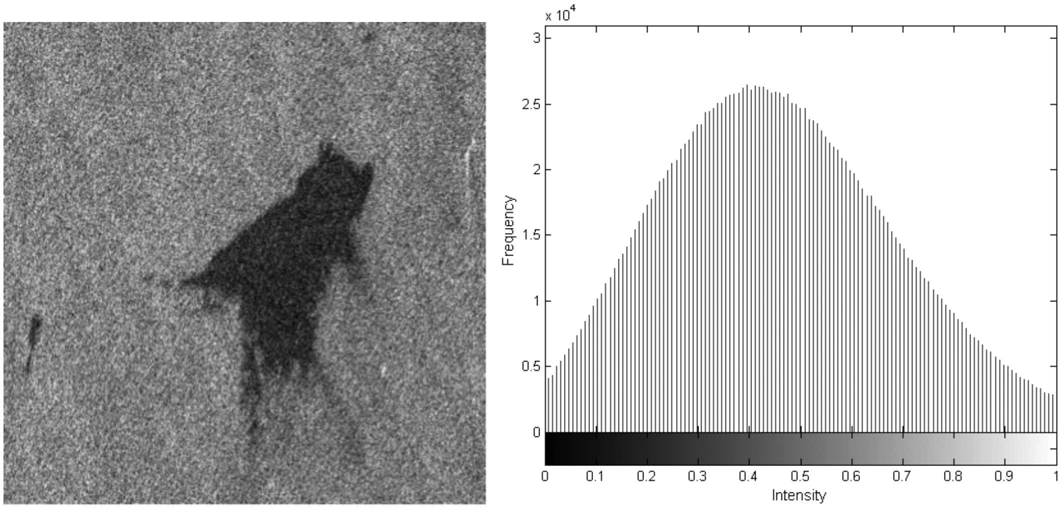

(a) (b)

Figure 3.1 (a) A subset from a typical SAR imagery, and (b) its corresponding histogram.

Automated segmentation approaches for SAR oil-spill and dark-spot detection can be categorized into two groups: (1) global segmentation schemes, and (2) local segmentation schemes.

There are numerous global segmentation schemes developed so far such as K-means clustering (Shi et al., 2007), global histogram thresholding (Otsu, 1979), and Gaussian mixture model (Alf et al., 2008). These global methods use the statistical distribution of pixel values from the entire image to segment the image into various regions. Thus, they do not perform particularly well with highly speckled SAR images since they are likely to ignore spatial relationships of neighbouring pixels. Due to underlying characteristics of these global methods they tend to be less prone to under- or over-segmentation issues, leading to a better capability of splitting dark regions and the background when speckles are properly treated. Several efforts have been made in the past to reduce or eliminate speckle noise presented in SAR images using adaptive filters such as Lee (Lee, 1980), Frost (Frost et al., 1982), and Kuan (Kuan et al., 1987). These SAR denoising filters are typically treated in the preprocessing step prior to the implementation of global segmentation methods to optimize the results.

Local segmentation methods such as region-growing (Lira & Frulla, 1998), level-set segmentation (Chan & Vese, 2001), Markov Random Field (Pelizzari et al., 2007), neural network (Topouzelis et al., 2008), marked point process (Li & Li, 2010), and spatial density thresholding (Shu et al., 2010) are based on the spatial and tonal relationships between pixels and are more robust in the presence of speckle noise. This is very critical as SAR images typically carry vast amounts of speckle. On the other hand, because local segmentation methods extract spatial and tonal characteristics locally, they are more prone to under- and over-segmentation problems. In the case of classical region-growing methods, results are not always promising as this method heavily depends on the initial selection of seed points from which it examines the neighbouring pixels as to whether to add to the region label or not. Similarly, a level-set segmentation method that detects edges by solving a partial differential equation is not robust to boundary gaps, and usually takes a great number of iterations to arrive at a satisfactory result. Equally important to note is that these local segmentation methods are generally rich in computation. For instance, the marked point process approach takes approximately 30 minutes to detect dark-spots on a 512 x 512 image using a PC-MATLAB platform indicating it is not well suited for practical use (Li & Li, 2010).

The main contribution of this paper is to combine the advantages of both global and local segmentation methods to minimize the effect of speckle noise and to better identify the dark-spot targets from the background. This can be realized by implementing the proposed novel approach of total variation optimization segmentation (TVOS) that first enforces two penalty terms to estimate the piecewise smooth state of the image and subsequently classifies it in a desired fashion. This paper is organized as follows: The underlying principle of the proposed method is described in Subsection 3.2. Subsection 3.3 presents and discuses the experimental results including data description, application of the proposed method on both synthetic image and operational COSMO-SkyMed image, and quantitative analysis and comparison with other well-established methods via kappa coefficient values. Finally, conclusions are addressed in Subsection 3.4.

3.2 TVOS Algorithm

The proposed TVOS approach can be divided into two main phases: (1) the total variation optimization phase, which is to provide a rough estimate of the piecewise smooth state. This is, "a clean state" based on two sets of constraint penalties; and (2) the finite mixture model classification phase, which is consequently applied to classify various features. In our case, either dark-spots being potential oil-spills or background being seawater are classified based on the result obtained in the first phase. As such, this two-phase algorithm can become a complete segmentation scheme to well reflect the task of dark-spot detection using SAR imagery.

3.2.1 Total Variation Optimization Phase

As is true with typical SAR imagery, the observed SAR image consists of many non-piecewise smooth regions whose classes are very difficult to separate due to many artifacts, inherent signal noise, and other image characteristics including the environmental conditions at the time of acquisition that in whole lead to a unimodal shaped curve indicating that there appears to be only one class as shown in Figure 3.1(b). Thus, the main objective of the total variation optimization phase is to obtain an initial estimate of the segmented image (denoted as *f),* given the observed SAR image (denoted as *g,)* by optimizing the energy function *E*. This inverse problem can be solved in many ways and one approach is to utilize the Rudin-Osher-Fatemi Total Variation (ROFTV) model and this can be expressed as follows;

$$g = f + u \,. \tag{3.1}$$

where u represents the residual state of the observed image. Based on this ROFTV model, the segmented image f will be forced to have multiple sets of piecewise smooth regions as total variation of f is minimized so that the classes in the image can be separated in a more efficient fashion. It is important to emphasize that while estimating the piecewise smooth state of *f*, the total variation minimization helps maintain the sharpness of the boundaries of the subject areas to preserve the original structure of the image by allowing for discontinuities (Evans & Gariepy, 1992). With the aid of the total variation minimization, we can theoretically achieve the segmented image where classes are well distinguished. With the additive relationship observed in equation (3.1), the problem of image segmentation can be formulated into the following minimization problem according to the ROFTV model (Rudin et al., 1992):

$$\hat{f} = \arg\min_f \left[\alpha \int_\Omega |f-g|^2 \, d\underline{x} + \beta \int_\Omega |\nabla f| \, d\underline{x} \right] \tag{3.2}$$

where Ω is an open set representing the image domain and ∇f represents the finite intensity difference between neighboring pixels. This is particularly important since it helps to avoid degradation of the edges and maintain sharp boundaries by investigating the intensity difference from surrounding pixels. The first term of equation (3.2) is the data fidelity term while the second term is the total variation term to enforce piece-wise smoothness in *f*.

It is well understood that by penalizing the intensity difference term, boundaries and edges are likely to be preserved since their intensity values are significantly different from the surroundings (Tomasi & Manduchi, 1998). However, the challenging task when dealing with SAR imagery is the handling of speckle noise in an effective manner. To tackle this challenging task one can use the spatial characteristics of pixels to help alleviate speckle noise since they are less correlated than the actual signal values, making it very robust to the presence of noise. Based on the aforementioned characteristics of taking both intensity and spatial characteristics of pixels that will ideally give an optimal segmentation result, the existing ROFTV model has been modified by adding another total variation penalty term called the spatial difference term to enforce the spatial closeness between surrounding pixels so that inherent image noise can be efficiently removed to a great extent. With the aid of the pre-existing intensity difference term and the additional spatial difference term, ∇x, to be included in the modified ROFTV model, the boundaries of the subject targets will be better preserved. In addition, the target will be minimally interrupted by the presence of speckle noise by enforcing spatial closeness of pixels as spatially distant pixels have less likelihood of belonging to the same dark regions. Hence, the dark-spot detection segmentation problem can be reformulated based on the proposed ROFTV model and it can be described as follows,

$$\hat{f} = \operatorname{argmin}_f \left[\alpha \int_{\Omega} |f - g|^2 \, d\underline{x} + \beta \int_{\Omega} \left(|\nabla f| + |\nabla x| \right) d\underline{x} \right] \tag{3.3}$$

Notice the additional spatial difference term has been included to better deal with speckle noise embedded in the SAR image and to force the piecewise smoothness of *f*. With this additional penalty term along with the existing intensity difference term, our modified ROFTV model will be able to efficiently and effectively handle the noise while preserving most of the details that were hidden in the image. In order to solve the above equation (3.3) and to obtain the segmented result, *f*, in a more efficient manner, we have utilized an iterative weighted optimization strategy that can be expressed by

$$\hat{f}_t = Z \int_{\Omega} \exp\left[\beta \left(|\nabla f| + |\nabla x| \right) \right] \hat{f}_{t-1} \, d\underline{x} \tag{3.4}$$

where Z is a normalization term and β is the regularization constant, $\beta = -1/\sigma$. This constant value was determined to provide the best result based on experimental testing both with synthetic and actual SAR images. In the course of this iterative weighted optimization strategy, the segmented result, *f,* gets iterated by taking both spatial closeness, ∇x, and the intensity difference, ∇f, among neighbouring pixels to better estimate the piecewise smooth state whose updated *f* is represented as $\hat{f}_t$ at iteration *t*. However, achieving the convergence of the optimization details of the piecewise smooth state can be very expensive from a computational perspective. To remedy this, experiments on the number of iterations of the optimization phase were conducted and it was consequently found that just one or two iterations were sufficient for achieving a satisfactory degree of piecewise smoothness of the image. Once such a state is achieved, the image should have well-separable statistical distributions by forming a multimodal shape of curve in its histogram as shown in Figure 3.2.

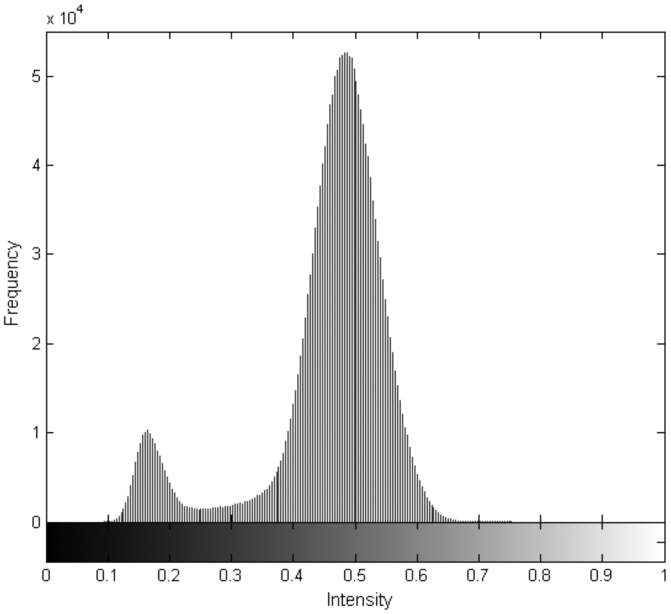

Figure 3.2 Bimodal statistical distribution of the approximated piecewise state drawn from Figure 3.1(a).

As illustrated in Figure 3.2, the statistical distribution of the original image containing a unimodal curve as shown in Figure 3.1(b) has changed to a bimodal curve indicating that the image noise has been significantly removed and the structure of the original image has been reconstructed such that classes are now easily separable. Note that the size of a processing window used for the testing was set to 9 x 9 when considering the original image size of 1,200 x 1,200 pixels. A processing window size is selected through the course of many experiments that for the image size between 1,000 x 1,000 pixels and 1,500 x 1,500 pixels, processing window of 9 x 9 was found to be sufficient. If the smaller image is used, then it should be tuned down to 7 x 7 or 5 x 5 for an optimal result. Motivated by the observation shown in Figure 3.2, a faster global finite mixture model classification scheme has been incorporated in the second phase to obtain the final segmentation result based on the product of the first phase of the proposed TVOS algorithm.

3.2.2 Finite Mixture Model Classification Phase

In the second phase of the proposed approach, a finite mixture model classification strategy was integrated to efficiently determine the final segmentation result. By investigating the overall statistical characteristics of the test datasets, the pixel pattern was observed to follow a Gaussian distribution. Inspired by this observation, a Gaussian mixture model was employed to find the number of classes existing in the subject image as well as their associated parameters through the course of the approximation of the piece-wise smooth state $\hat{f}$. This set of parameters to be estimated using the Gaussian mixture model is denoted by Θ,

$$\Theta = \left\{\mu_1, ..., \mu_n, \sigma_1, ..., \sigma_n, \pi_1, ..., \pi_n\right\} \tag{3.5}$$

where μ, σ, and π represent the mean, standard deviation, and probability of a component within the mixture model, respectively. Let n be the number of components within the mixture model, and *l* be a class label where *l* ∈ {1, ..., n}. Then the probability of observing the estimated $\hat{f}$ can be expressed by the following equation,

$$p\left(\hat{f}\middle|\Theta\right) = \sum_{i}^{n} p\left(\hat{f}, l = i\middle|\Theta\right) \tag{3.6}$$

Due to the nature of Θ often being intractable to solve, we perform an expectation maximization (Dempster et al., 1977) strategy to estimate the parameters that are essential prior to arriving at the final step to classify subject targets in a desired fashion. For this, an iterative expectation maximization approach is performed to estimate Θ as expressed by

$$\Theta_{t+1} = \text{argmax}_{\Theta} \sum_{j=1}^{v} \sum_{i=1}^{n} p\left(l_j = i\middle|\hat{f}_j, \Theta_t\right) \ln p\left(l_j = i\middle|\hat{f}_j, \Theta\right) \tag{3.7}$$

Such a task can be accomplished by iteratively processing two steps: an expectation (E) step to calculate the log likelihood function to predict the associated parameters, and a maximization (M) step to find such parameters that maximize the expected log-likelihood function determined in the previous E step. Once associated parameters are calculated via EM for the Gaussian mixture model, the maximum likelihood classification technique can be implemented to assign the final class, being either dark-spots or background at pixel $\underline{x}$ by solving the following,

$$\hat{l}(\underline{x}) = \arg\max_l p\left(\hat{f}(\underline{x})|l\right) \tag{3.8}$$

Once the product of the first phase undergoes the processing in the second phase of the TVOS algorithm, the possible dark-spots should theoretically be found while leaving others (non dark-spots) in the background.

3.3 Results and Discussion

3.3.1 Description of Data and Comparison Methods

The scene was captured by Italian X-band SAR imaging satellite, COSMO-SkyMed. Unlike some other SAR sensors that have low spatial and temporal resolution, COSMO-SkyMed has a frequent revisiting time and high spatial resolution. The image used in this paper is a stripmap product whose spatial resolution is 3 m with a swath width of 40 km. It operates in X-band at 9.6 GHz with VV polarization mode. Date and time of acquisition are 10:46:03 am on the 9th September 2009 and the size of the image is 20,748 x 21,276 pixels. SAR images recorded by COSMO-SkyMed can be an ideal option for oil-spill monitoring as many studies have proved the effectiveness of using SAR sensors equipped with shorter wavelength, such as X-band, for such applications (Trivero et al., 2007; Kim et al., 2010). This image was taken in the ocean nearby the City of Qingdao, Shandong province, China and it contained verified oil-spills as can be confirmed by the airphoto taken on the scene (see Figure 3.3).

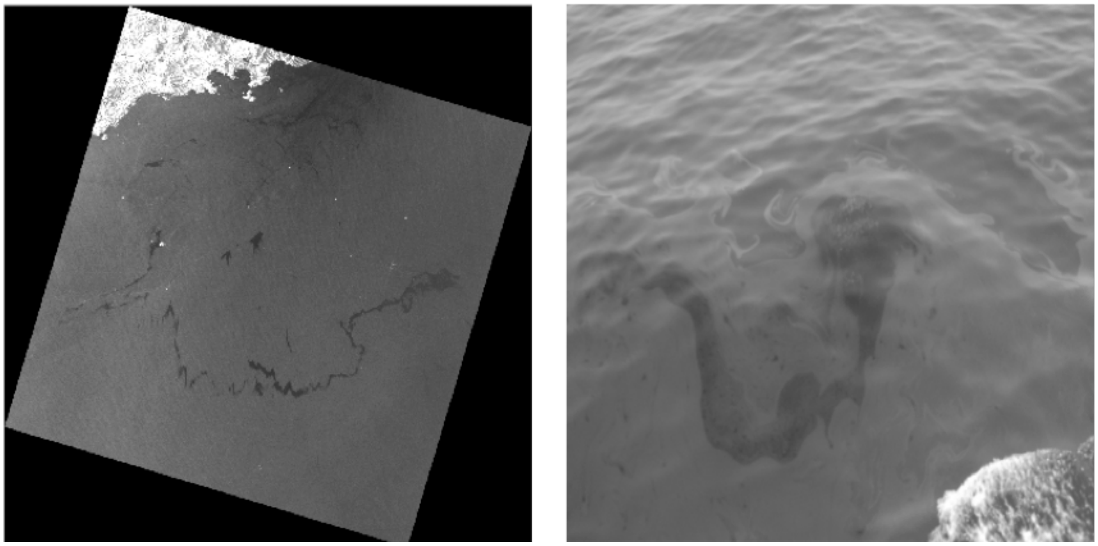
(a) (b)

Figure 3.3 (a) A scene of oil-spills captured by COSMO-SkyMed, and (b) verified by an airphoto.

As shown in Figure 3.3, verified oil-spills appear as dark regions due to the dampening effects which cause less backscattering to be recorded by the SAR antenna. Overall, this image is a good candidate to conduct research with since it is preset to an optimal setting including SAR sensor settings and verified oil-spills for testing the proposed method used for oil-spill detection.

In this study we have performed two different tests: (1) Test I using synthetic data under varying noise, and (2) Test II using real COSMO-SkyMed SAR imagery containing verified oil-spills. To show the robustness and effectiveness of the proposed method we have also included comparison studies with other widely used methods, particularly for SAR image segmentation. Lee & Jurkevich (1989) investigated the feasibility of a SAR segmentation scheme when they implemented Lee's adaptive filter to remove the speckles in an image and employed global histogram thresholding, known as Otsu, to split the target from the background. The results drawn from utilizing such an algorithm indicates its robustness. Another SAR segmentation framework developed by Marques et al. (2004), similar to Lee and Jurkevich's, combined the aforementioned denoising filters, such as Kuan with the K-mean clustering method, and the results were found to be very promising. Two very similar segmentation frameworks were tested and the results were found to be very similar as expected when considering two-class segmentation in which both K-means and Otsu would normally produce similar results. Thus, only the results obtained by using Kuan + K-means were included as this method is newer and has been widely used until now. Another method used to compare with the proposed method is based on the level-set segmentation method proposed by Chan & Vese (2001) and was chosen since its performance has proven to be outstanding for SAR images (Lu et al., 2009). Lastly, the original ROFTV model, which contains only the intensity difference term, followed by the 2nd phase of the proposed method (hereinafter referred to as ROFTV method) was included to see how much improvement the proposed TVOS method could make in comparison with the original ROFTV method.

3.3.2 Experiment using Synthetic Imagery under Noise

The performance of the proposed TVOS method was investigated using an artificially created image. This image was created with two classes, dark regions being possible oil-spills and backgrounds being seawater as shown in Figure 3.4.

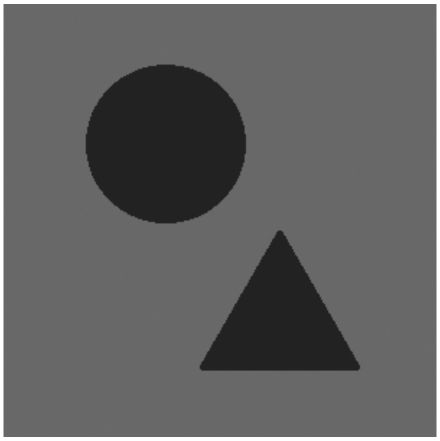

Figure 3.4 Synthetic Dark-spot Image.

To make the data similar to a typical SAR data, 15 different levels of multiplicative noise, σ^2, have been added ranging from 0.01 to 0.70 whose values increase at an increment of 0.05. Due to the lack of space, only the test images containing artificial multiplicative noise with a variance of 0.01 being low, 0.25 being mid-low, 0.45 being mid-high, and 0.70 being high have been displayed in this paper. Figure 3.5 illustrates the comparison of segmentation results via three other methods and the proposed TVOS as mentioned earlier. To optimize the visibility, the segmentation results are outlined in black contours.

As can be seen from Figure 3.5, the proposed TVOS method outperformed the other three methods as shown by comparison of segmentation results. Although local segmentation methods, such as the level-set method, are known for their robustness in the presence of speckle noise, this synthetic testing proved that they were still fragile in their denoising capability when dealing with highly speckled images leading to poor segmentation results.

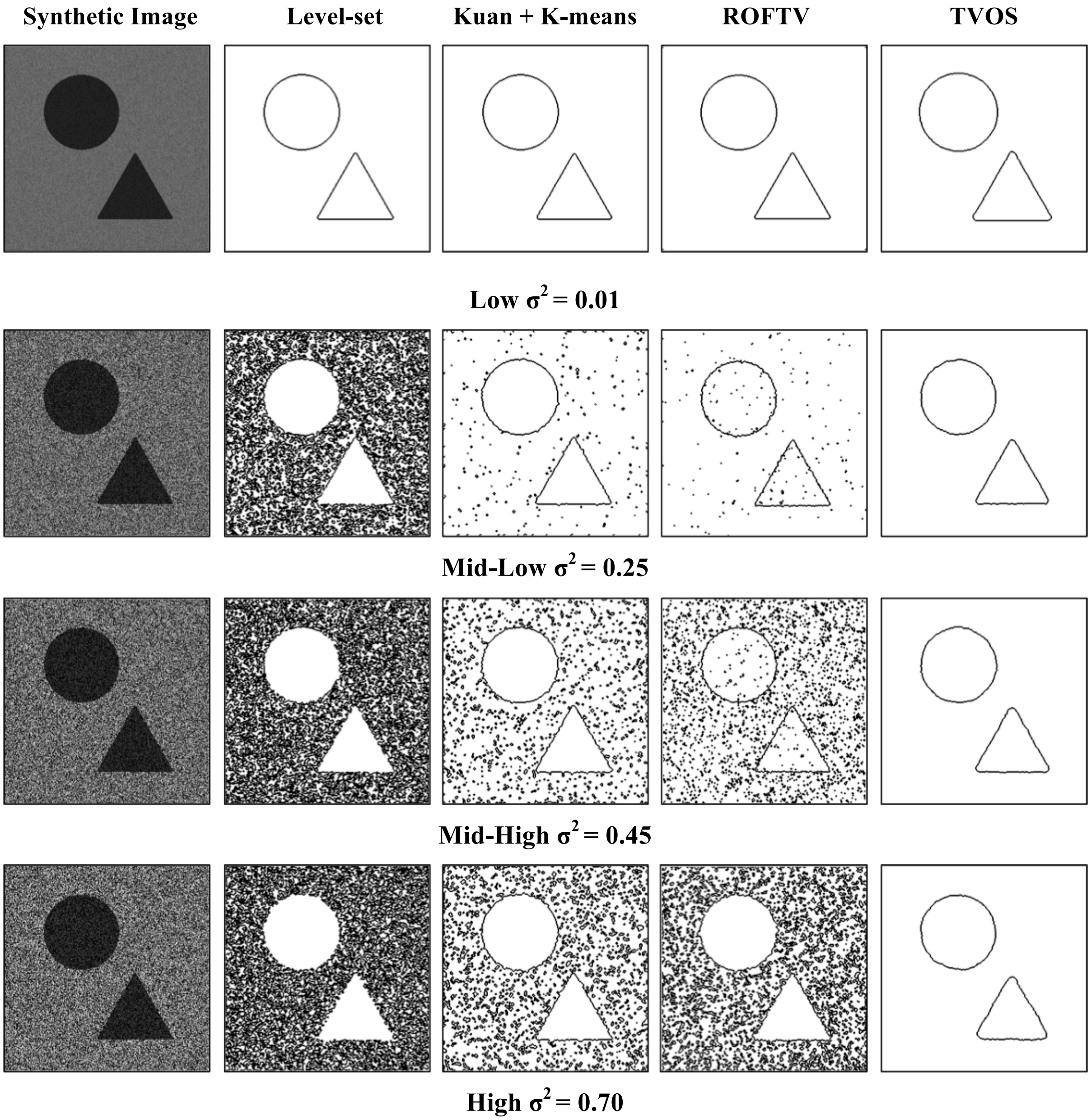

Figure 3.5 Comparison of segmentation results via level-set, Kuan + K-means, ROFTV, and TVOS at four different levels of multiplicative noises.

Segmentation results drawn from the global K-means clustering method combined with local Kuan's adaptive filter produced relatively better results than that of level-set's. Theoretically, this combined method should perform better as it accounts for advantages from both global and local based methods, with its strength in denoising capability and being less prone to under- or over-segmentation issues. However, as the severity of speckle noise increased, the combined method failed to achieve a satisfactory result. In addition, the segmentation results drawn from use of the ROFTV method indicated its poor segmentation performance. It is important to emphasize that homogeneity within a region was not enforced and speckles were not sufficiently treated due to the absence of the spatial difference penalty term. On the other hand, the proposed TVOS method constantly well segmented the two distinct classes in a wide range of varying speckle noise in a desired manner. Such satisfactory results were obtained due to two penalty terms that were incorporated into the existing ROFTV model. The spatial difference penalty term removed the speckle noise to a great extent and the intensity difference penalty term preserved the boundaries of the subject areas. Hence, the segmentation results using an artificially created synthetic image under different noise levels display the effectiveness and robustness of the proposed TVOS method.

3.3.2.1 Quantitative Data Analysis on Synthetic Image

Cohen's kappa coefficient analysis is well known, particularly in remote sensing communities, for providing a robust measure of segmentation results. It is believed to be a more effective measure than a simple percentage measurement since it takes the random agreement by chance into account. The equation for Cohen's kappa coefficient, κ is as follows (Cohen, 1960);

$$\kappa = \frac{p_o - p_c}{1 - p_c}, \tag{3.9}$$

where P_o is the proportion of observed percentage agreement and P_c is the proportion of overall probability of random agreement. The coefficient, κ, ranges from 0 being a totally incomplete agreement and 1 being a complete agreement. Thus, better segmentation results will yield to a kappa coefficient close to 1. Figure 3.6 summarizes the kappa coefficients obtained from three different methods of segmentation results in a graphical representation.

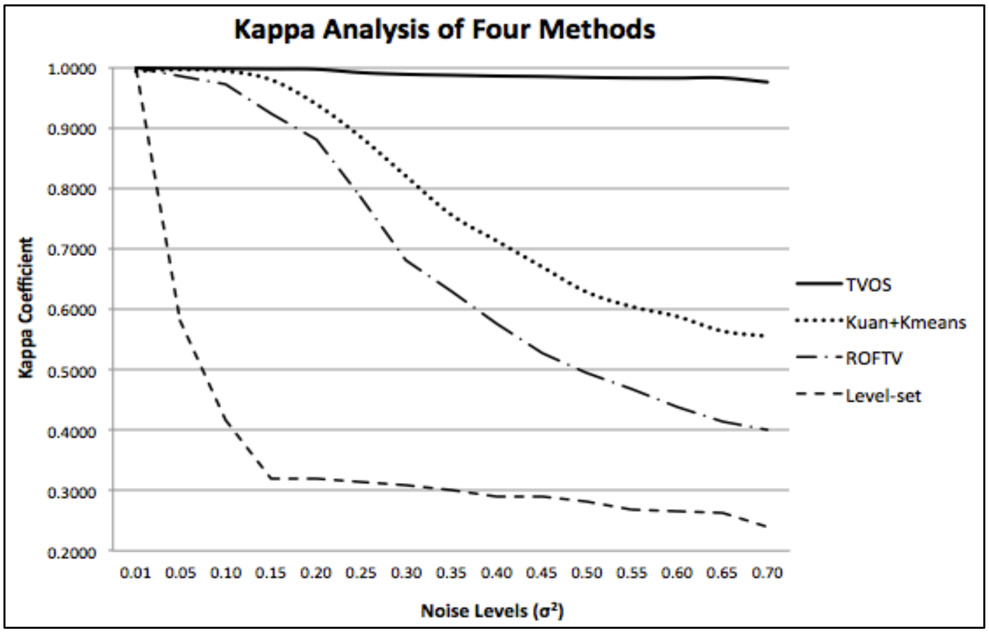

Figure 3.6 Kappa coefficients from four segmentation methods under different noise levels.

Figure 3.6 illustrates the outstanding segmentation performance of the proposed TVOS method since the kappa values constantly reach near 1. This indicates the segmentation results are very well matched with the original synthetic test image. In contrary, kappa values for segmentation scheme based on the level-set method are very poor as was expected through the visual inspection as discussed in the previous section. It produced a comparably good result at the low speckle, $\sigma^2 = 0.01$, however, starting from $\sigma^2 = 0.15$ it quickly loses its robustness and the ability of segmentation gets uncompromisingly worse at higher noise levels. Kappa coefficients for the Kuan + K-means method show relatively better results with some stability up to mid-low range levels. As the weight of speckle noise increases, Kuan's adaptive filter became insufficiently strong in removing the speckle noise resulting in a poor segmentation output. The results of the ROFTV method did not produce a satisfactory outcome, which was evident when investigating the kappa coefficient values that formed a constant decreasing pattern. On the other hand, the proposed method produced a robust segmentation performance throughout all different noise levels with its two total variation constraints taken into account. This is a good example showing how much difference the absence of spatial difference could bring in terms of its overall segmentation performance. An additional experiment was conducted to further investigate the robustness of the proposed method by applying higher noise values until the proposed method began to fail the separation of two classes. As a result, the kappa coefficient values were found to drop below 0.9, 0.8, and 0.7 starting at σ^2 = 3.5, 4.3, and 4.8, respectively.

Thus, a quantitative measure of kappa coefficients has once again confirmed the superiority of the proposed TVOS algorithm for its solid segmentation ability under wide ranges of different noise levels.

3.3.3 Results using COSMO-SkyMed Imagery

In this section, segmentation results obtained by three comparison methods (level-set, Kuan + K-means, and the ROFTV method) and the proposed TVOS method on a real COSMO-SkyMed image are presented and discussed. Due to its large size, the original image was subsetted into 46 smaller test images with different sizes to make the tests more efficient. Of those 46 tested images, only the results derived from five subsets are included in this paper due to a limited space. It is important to note that all of these tested datasets contained verified oil-spills. Figure 3.7 shows the original subsetted COSMO-SkyMed images and the segmentation results drawn from the above-mentioned four methods.

The segmentation results obtained using the proposed TVOS algorithm clearly stand out when compared to the results of the three comparison methods. Such astounding results were obtained mainly due to the combination of both local- and global-based segmentation schemes. Local-based schemes built in the TVOS algorithm use two penalty terms to enforce a piecewise smooth state of the image by eliminating speckle noise effectively without removing the fine details in the original observed SAR imagery, including boundaries of the target area. A global-based segmentation scheme in TVOS correctly extracts the subject target (dark-spots) from the background (seawaters). On the other hand, results from the level-set segmentation method failed to produce satisfactory results. In addition, with the experimental results obtained from the previous section using a synthetic image we can conclude its ineffectiveness in a highly speckled environment. Kuan + K-means managed to produce a relatively better segmentation result than that of level-set's, although the results still contained many wrongly classified pixels. The ROFTV method produced poor segmentation results due to the absence of the spatial difference term that the speckles were insufficiently treated and the homogeneity within a region was not adequately enforced.

For any segmentation method to go beyond the prototype stage and be used in real world applications, the processing time is considered very important. In this aspect, the TVOS algorithm managed to complete the task in a timely manner while level-set segmentation method produced unsatisfactory results after a long processing time. For example of the test image 1 on a PC-based MATLAB platform, the proposed TVOS algorithm took 32 seconds while the ROFTV method and level-set took 35 seconds and 14 minutes, respectively to complete the same segmentation task. Although a fewer number of constraints were added into the ROFTV method in comparison with the proposed TVOS method, the ROFTV method still took 3 seconds longer because the 2nd phase of the ROFTV method needed additional time to estimate the final class likelihoods using poorly distributed pixels. Kuan + K-means took the shortest processing time of all, however the segmentation results were compromised at the expense of a quick processing time. The processor of the computer used for experiments was an Intel dual core CPUs at 2.4 GHz with 3GB of RAM. Although the TVOS algorithm is designed to evolve iteratively until the desired results are achieved, considering the relative simplicity of two-class segmentation, only one iteration of total variation optimization phase was sufficient to achieve a “clean” result. In comparison, level-set took 63 iterations to get its final product. As such, the overall superior qualities of the proposed TVOS algorithm well demonstrate the effectiveness and robustness in producing a promising and accurate segmentation result in a timely fashion.

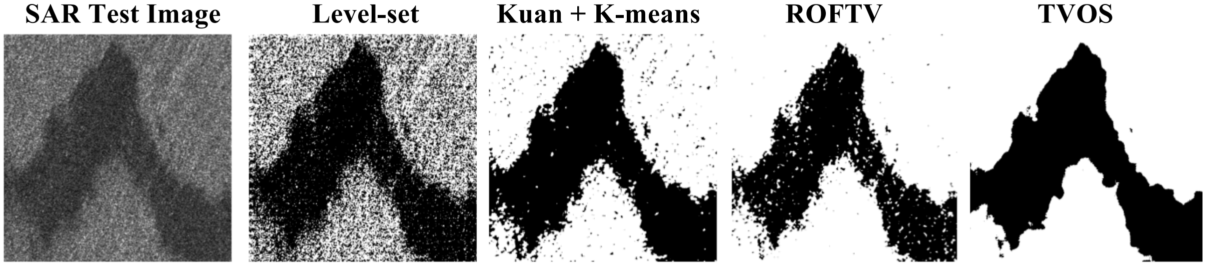

Test 1: Image size [600 x 600]

Test 2: Image size [700 x 700]

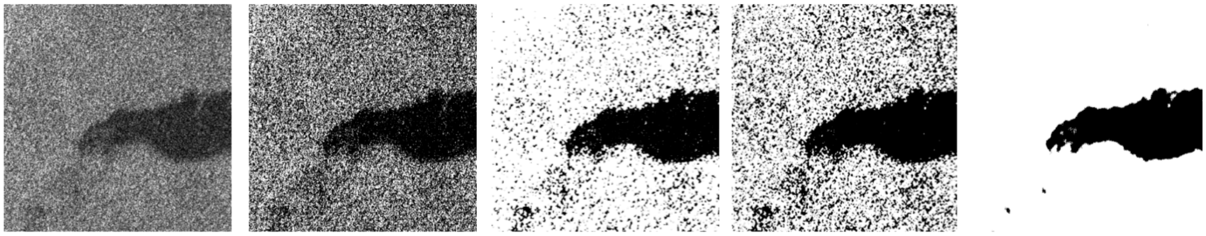

Test 3 Image size [800 x 800]

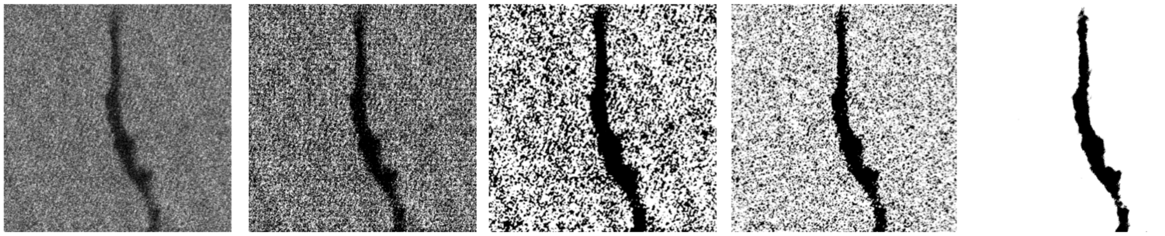

Test 4 Image size [900 x 900]

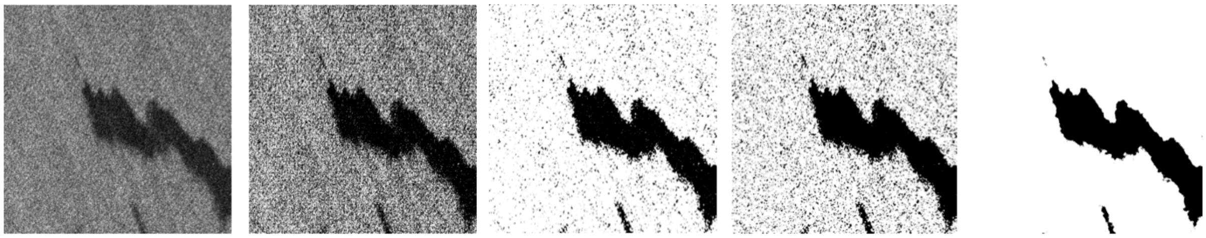

Test 5 Image size [1100 x 1100]

Figure 3.7 Subsetted original SAR oil-spill images and the segmentation results by four methods.

3.4 Conclusions

The work presented in this paper focused on the critical step in oil-spill monitoring, which is to detect all the possible dark-spots present in an image. Thus, a novel dark-spot detection approach is proposed, namely the total variation optimization segmentation (TVOS). The TVOS algorithm first applies the spatial and the intensity difference penalty terms to minimize the total variation of the image and to obtain the rough estimate of the piecewise smooth state of the original noisy image. Once the classes in the image have become well separable, a purely global classification scheme is subsequently utilized to extract only the dark-spots from the background. To fulfill this task, an expectation maximization technique is implemented iteratively to estimate the parameters using the Gaussian mixture model. Then the maximum likelihood classifier is employed to estimate the final class containing only the dark-spots. The experiments both on a synthetic and real SAR oil-spill images showed that the proposed TVOS algorithm surpasses the performance of the rest of comparison methods. In addition, kappa coefficients of the segmented TVOS algorithm results using the synthetic testing images under noise were found to be near 1, indicating that its segmentation result mostly matches with its reference data whereas other methods do not. In addition, the processing time was relatively fast when compared to other conventional methods. Overall, the visual inspection as well as the quantitative analysis confirmed the proposed TVOS algorithm is fast, effective, and robust in detecting dark-spots in a highly speckled SAR imagery. Further research can be undertaken to improve the proposed method by adding other penalty terms, such as gradient or texture difference to better handle the segmentation task. Study on the utilization of dual or quad polarimetirc SAR imagery would be beneficial to help identify a dark-spot from the background as well.

Chapter 4

ETVOS: An Enhanced Total Variation Optimization Segmentation Approach for SAR Sea-ice Image Segmentation

Overview

This paper presents a novel enhanced total variation optimization segmentation (ETVOS) approach consisting of two phases to segmentation of various sea-ice types. In the total variation optimization phase, the Rudin-Osher-Fatemi total variation model was modified and implemented iteratively to estimate the piecewise smooth state from a non-piecewise smooth state (the original noisy imagery) by minimizing the total variation constrains. In the finite mixture model classification phase, based on the pixel distribution, an expectation maximization method was performed to estimate the final class likelihoods using a Gaussian mixture model. Then a maximum likelihood classification technique was utilized to estimate the final class of each pixel that appeared in the product of the total variation optimization phase. The proposed method was tested on a synthetic image and various subsets of RADARSAT-2 imagery and the results were compared with other well-established approaches. With the advantage of a short processing time, the visual inspection and quantitative analysis of segmentation results confirm the superiority of the proposed ETVOS method over other existing methods.

4.1 Introduction

Sea-ice condition monitoring in Polar Regions is very important for various applications, including scientific research, especially in the context of global climate changes. Sea-ice has a high albedo due to its color and the fact that most of the sunlight that interacts with the sea-ice surface is reflected back into the atmosphere resulting in cold climates in Polar Regions. The temperature in Polar Regions has been constantly increasing due to loss of sea-ice that has reduced the amount of sun rays reflected, causing sea-ice to melt and become weakened. This trend consequently leads to a bigger problem of global climate change that will cause severe consequences to human life and Earth's natural environment. Having acknowledged the importance of sea-ice monitoring, the amount of SAR sea-ice images acquired by Canada's RADARSAT-1 and -2 that are received daily at the Canadian Ice Service (CIS) and processed by trained sea-ice analysts is overwhelming. Hence there is a great need for an automatic sea-ice monitoring system.

One of the key advantages of using SAR for sea-ice monitoring is that it uses microwave rays in the electromagnetic spectrum (EMS), which can penetrate rain, clouds and other atmospheric substances, resulting in good monitoring capabilities during the day and night. Moreover SAR has proven to be the most important tool for the detection of sea-ice (Deng & Clausi, 2005). However the segmentation of SAR sea-ice images is a very difficult task due to the presence of a multiplicative noise known as speckle. Not only does speckle noise degrade the quality of SAR images, but also makes it a very challenging task to extract tonal and texture information from images. A good example of a SAR sea-ice image adversely affected by speckle noise is shown in Figure 4.1. Although there is a clear visible distinction between the two different classes, there seems to be no difference in statistical distribution of pixel values as shown in the unimodal shaped histogram.

If the statistical distribution of pixel values forms a unimodal shape, then accurate segmentation is not possible since a computer would recognize this image as containing only one class with similar intensity values. However, this is not true as there is an apparent difference observed from Figure 4.1(a). This behavior is believed to occur mainly due to the presence of speckle noise, which is the most influential contributing factor. Existing approaches available for automatic segmentation of SAR sea-ice images include K-means clustering (Redmund et al., 1998), dynamic local thresholding (Havercamp et al., 1993), Gamma mixture models (Samadani, 1995), Gaussian mixture model (Alf et al., 2008) , neural networks (Karvonen, 2004), and a global histogram thresholding (Otsu, 1979). These methods were developed based on the investigation of global tonal characteristics from the entire image and have drawbacks and weaknesses. Mechanisms built based on global tonal characteristics tend to ignore spatial relationships between pixels, making them very difficult to implement in a highly noise-contaminated image such as SAR sea-ice images. A local-based method, such as IRGS, utilizes edge penalties and region growing techniques to better preserve edges while efficiently separating different sea-ice types. This method tends to be more robust in dealing with speckle noise, but the fast processing speed can only be achieved at the expense of accuracy (Yu & Clausi, 2008). In addition, it is sometimes difficult to obtain a desirable classification result by employing the region-growing method since this classification method depends greatly on the selection of an initial seeding location.

Conventional yet robust denoising filters such as Lee adaptive filter (Lee, 1980), Kuan filter (Kuan et al., 1987), Frost filter (Frost et al., 1982) and speckle reducing anisotropic diffusion method (Yu & Acton, 2002) are widely used to denoise images prior to the application of a segmentation scheme and many of these filters are currently available in commercial image processing software packages. However, these methods do not perform well when dealing particularly with images that contain significant speckle noise.

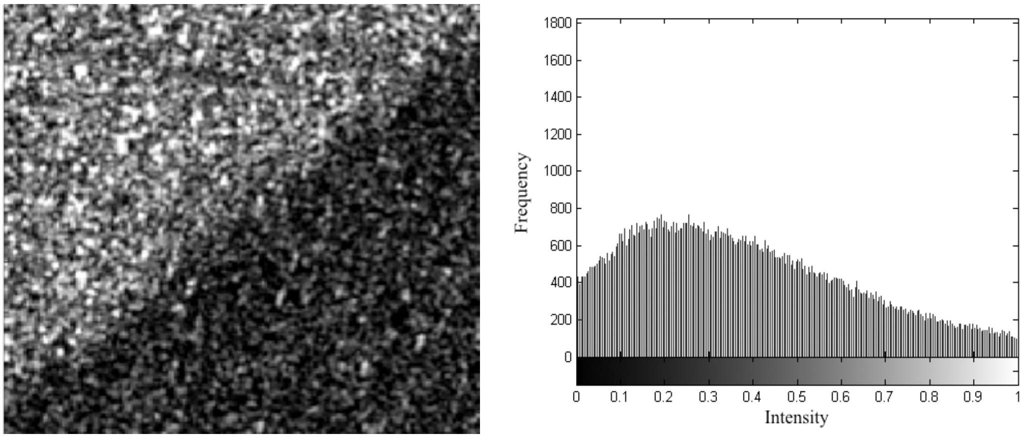

(a) (b)

Figure 4.1 (a) A subset of RADARSAT-2 sea-ice image, and (b) its corresponding histogram.

Apart from deriving a segmentation result by exploiting spatial and tonal relationships between pixels, other approaches to analyze texture characteristics have been studied as well (Barber & LeDrew, 1991; Clausi, 2002). Moreover, some of the texture-based approaches developed so far include gray-level co-occurrence probabilities (Chellappa & Chatterjee, 1985; Shokr, 1991; Nystuen, 1992) and Gaussian Markov random fields (Yu & Clausi, 2007). These texture-based segmentation schemes have the weakness that pixels located near texture boundaries are likely to be misclassified. More importantly, some of these methods can be computationally intensive resulting in longer processing times and therefore are not well suited for practical use. Thus, the main contribution of this paper is to use a novel enhanced total variation optimization segmentation (ETVOS) approach to first reconstruct the piecewise smooth state to be able to better separate the existing classes and to classify distinct features in a timely fashion.

The paper is organized as follows. The underlying methodology behind ETVOS is presented in Subsection 4.2. In Subsection 4.3, experimental results including data description and analysis, testing on a synthetic image, results and discussion of the proposed method, and comparison with other methods are addressed. Lastly, Subsection 4.4 provides a summary of the work done and recommendations for future work.

4.2 Methodology

The ETVOS method consists of two main phases: Phase I - extended total variation optimization, and Phase II - finite mixture model classification. In Phase I, a total variation optimization approach based on a set of constraint penalties is used to provide a rough estimate of the piecewise smooth state separating the classes in the original image. In Phase II, a finite mixture model classification strategy is employed on the results from Phase I to classify distinct features including land, seawater and various sea-ice types that appear in SAR sea-ice imagery. Thus the combination of the two phases together, a full and comprehensive segmentation algorithm, ETVOS can be realized.

4.2.1 Phase I – Extended Total Variation Optimization

SAR sea-ice segmentation can be formulated as an optimization problem, where the goal is to estimate the segmented image denoted as f given the observed SAR image denoted as g by optimizing the energy function E. One approach for solving this inverse problem is through the utilization of the Rudin-Osher-Fatemi Total Variation (ROFTV) model. Based on the ROFTV model, the observed SAR image g can be represented as a combination of the piece-wise smooth state f and residual state u, as given by

$$g = f + u \tag{4.1}$$

In other words, by utilizing the ROFTV model, the goal is to progressively evolve a non-piecewise smooth state g in which classes are nonseparable due to noise, artifacts, and other image details, into a piecewise smooth state f where the total variation of the image is minimized and the classes are well delineated. In the process of estimating such state, the total variation minimizers in the space of function of bounded variation help preserve edges or boundaries of the objects in the image by allowing for discontinuities (Darbon & Sigelle, 2005). Therefore, we are able to theoretically arrive at a clean state with sharp boundaries between different classes. Given the additive relationship in equation (4.1), the problem of image segmentation can be formulated into the following minimization problem based on the ROFTV model (Rudin et al., 1992),

$$\hat{f} = \arg\min_f \left[\alpha \int_\Omega |f - g|^2 \, d\underline{x} + \beta \int_\Omega |\nabla f| \, d\underline{x} \right] \tag{4.2}$$

where Ω is an open set representing the image domain, and ∇f represents the finite intensity difference between neighboring pixels. The first term of equation (4.2) is the data fidelity term, while the second term is the total variation term that penalizes pixel intensity differences within regions to enforce piece-wise smoothness in *f*.

It is well understood that by penalizing pixel intensity differences with its immediate neighbors, the edges or boundaries of the objects are better preserved but is limited in handling high noise levels. To remedy this limitation, one can take spatial closeness of pixel values into account via extending the spatial neighborhood being considered to improve statistical resilience to noise, as well as incorporating of a spatial penalty term that enforces spatial closeness between pixels in a variable manner. Furthermore, to further improve boundary preservation while maintaining efficiency, an additional penalty term that penalizes gradient differences can be incorporated into the ROFTV model, as large gradient differences are indicative of boundary crossings between two classes or regions.

Based on the aforementioned motivations, in the proposed ETVOS approach, we extend upon the existing ROFTV model with two additional total variation penalty terms: i) a penalty term that enforces spatial closeness, and ii) a penalty term that penalizes gradient differences. These additional penalty terms are incorporated to better reflect the task of SAR sea-ice image segmentation, where we wish to preserve the boundaries between different sea-ice types under the presence of high speckle noise. The first total variation penalty term introduced into to the extended model is the spatial difference term denoted by $|\nabla \mathrm{x}|$, which enforces spatial closeness since spatially distant pixels are less likely to belong to the same sea-ice region. The second penalty term introduced into the extended model is the gradient difference term denoted by |∇k|, which enforces low gradient differences since pixels with large gradient differences are less likely to belong to the same region. Therefore, with these additional constraints, the final formulation of the segmentation problem based on the proposed extended ROFTV model can be written as

$$\hat{f} = \operatorname{argmin}_f \left[\alpha \int_\Omega |f - g|^2 \, d\underline{x} + \beta \int_\Omega \left(|\nabla f| + |\nabla x| + |\nabla k| \right) d\underline{x} \right] \tag{4.3}$$

As can be seen in equation (4.3) the spatial and gradient penalty difference terms have been incorporated to extend the ROFTV model to better estimate the piecewise smooth state where classes can be easily separable. To solve this problem in an efficient manner, an iterative weighted optimization strategy is employed to approximate *f*, where the updated estimate $\hat{f}_t$ at iteration *t* can be expressed by

$$\hat{f}_t = Z \int_\Omega \exp\left[\beta \left(|\nabla f| + |\nabla x| + |\nabla k| \right) \right] \hat{f}_{t-1} \, d\underline{x} \tag{4.4}$$

where Z is a normalization term and β is the regularization constant. Based on testing, it was found that $\beta = -1/\sigma$ provided strong results across different sets of data.

Theoretically, running the optimization detailed in equation (4.4) to convergence would provide us with the piecewise smooth state that represents the segmented image *f*. However, from a practical perspective, running this strategy to convergence to achieve steady state can be computationally expensive. However, throughout the course of numerous tests, it has been found that even running a limited number of iterations can provide good approximations of the piece-wise smooth state. Furthermore, from Figure 4.2, one can see from the statistical distribution of pixel values in the approximation of the piece-wise smooth state for the scene (shown in Figure 4.1(a)) that this approximation of the piece-wise smooth state has a multimodal shape, meaning that a faster alternative global classification strategy can now be employed on the results from Phase I to determine the final segmented results. Motivated by this observation, the proposed method utilizes a finite mixture model classification strategy in the second phase to determine the final segmented results based on the results from Phase I.

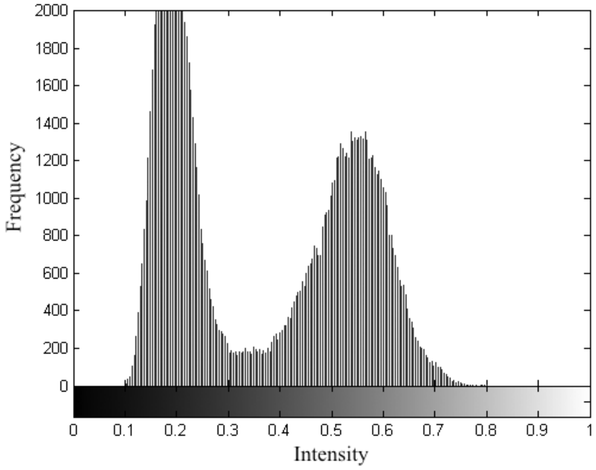

Figure 4.2 Histogram generated from the approximation of the piece-wise smooth state for the scene shown in Figure 4.1(a).

4.2.2 Phase II – Finite Mixture Model Classification

In Phase II, a Gaussian mixture model (GMM) is employed to find how many different classes there are and their associated parameters in the approximation of the piece-wise smooth state $\hat{f}$. Let n be the number of components within the mixture model. Furthermore, let l be a class label where $l \in \{1, ..., n\}$, and Θ be the set of parameters to be estimated for the mixture model,

$$\Theta = \left\{\mu_1,...,\mu_n,\sigma_1,...,\sigma_n,\pi_1,...,\pi_n\right\} \tag{4.5}$$

where μ, σ, and π denote the mean, standard deviation, and probability of a component within the mixture model, respectively. Given such a model, the probability of observing $\hat{f}$ can be expressed by

$$p\left(\hat{f}\middle|\Theta\right) = \sum_{i}^{n} p\left(\hat{f}, l = i\middle|\Theta\right) \tag{4.6}$$

To estimate Θ, expectation maximization (EM) (Dempster et al., 1977) is performed as follows,

$$\Theta_{t+1} = \text{argmax}_{\Theta} \sum_{j=1}^{v}\sum_{i=1}^{n} p\left(l_j = i\middle|\hat{f}_j,\Theta_t\right)\ln p\left(l_j = i\middle|\hat{f}_j,\Theta\right) \tag{4.7}$$

Finally once the parameters of the mixture model are formed by utilizing EM, the maximum likelihood estimate of the final class l at pixel $\underline{x}$ can be determined as

$$\hat{l}\left(\underline{x}\right) = \arg\max_l p\left(\hat{f}\left(\underline{x}\right)\middle|l\right) \tag{4.8}$$

4.3 Experimental Results

A RADARSAT-2 image covering the ocean nearby the Island of Newfoundland in Canada was used in this study since it contained various sea-ice types that have been verified by trained sea-ice analysts at CIS. The image was acquired in the HH polarization mode using ScanSAR Wide beam at 22:29:36 on March 16, 2009 and its spatial resolution had been degraded to 100 m for the enhancement of sea-ice, which is ideal for sea-ice detection. Due to a large size of the original image (4239 by 4221 pixels), a smaller subset of this image was used to enable a relatively shorter processing time. To have a better understanding of the dataset, a Google map was referenced to help distinguish land, ocean and sea-ice, which have been labeled accordingly as shown in Figure 4.3.

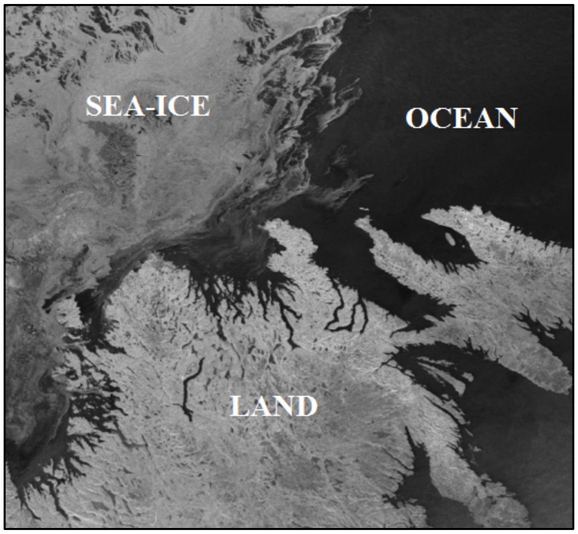

Figure 4.3 RADARSAT-2 Sea-ice image containing three main features.

To validate the proposed algorithm in detecting various sea-ice types in a more convincing fashion, analytical data that confirms sea-ice types was necessary. The CIS website has an archive in which weekly regional ice charts are available. Fortunately the regional ice chart covering the subject dataset was available. The regional ice chart also provides the series of egg-codes in a simple oval form, which details the sea-ice concentrations, stages of development, and form of the ice for each segment of sea-ice covered regions as shown in Figure 4.4 (Environment Canada, 2011). By carefully analyzing the egg-codes for each segment of the study area, it was found that there were mainly two different types of sea-ice presented; (1) “Egg-Code 4” representing grey ice with a thickness of 10-15 cm, and (2) “Egg-Code 1.” representing medium first-year ice with a thickness of 70-120 cm (Environment Canada, 2011).

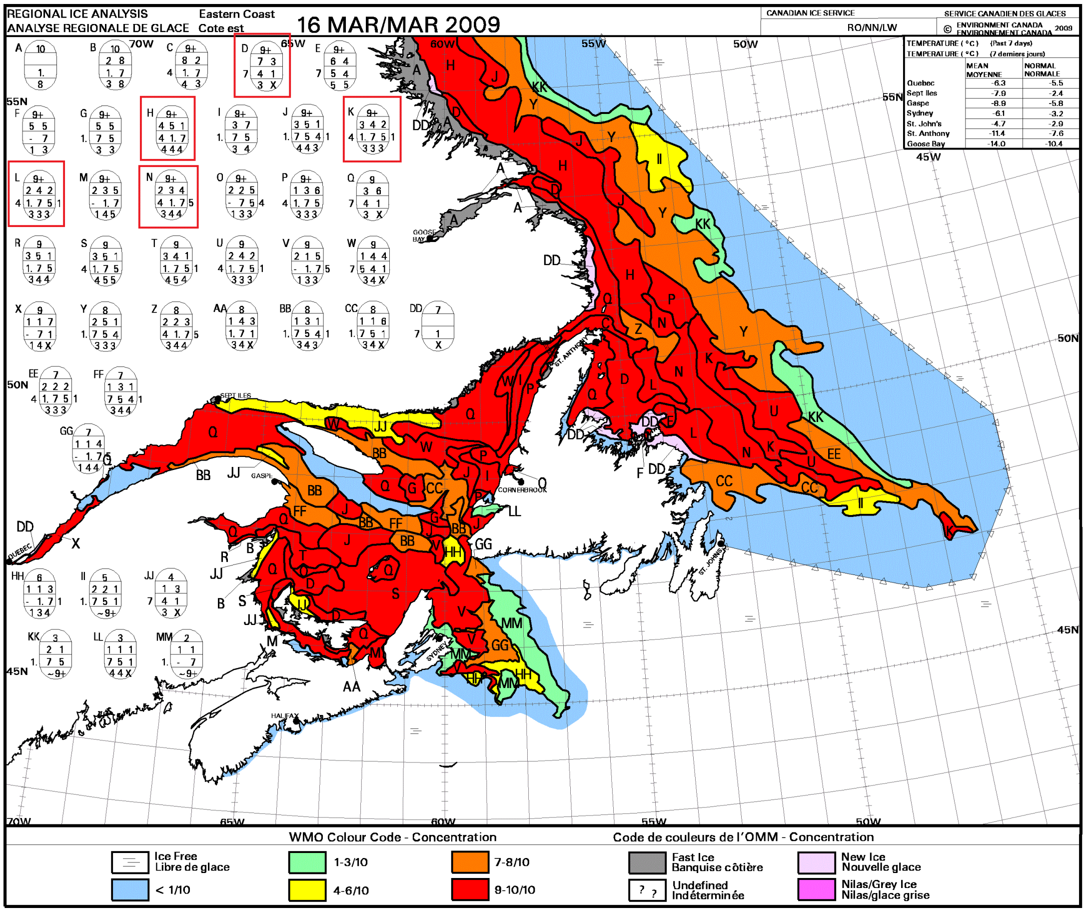

Figure 4.4 Daily Sea-ice Chart with Egg-Codes (Environment Canada, 2011).

However, the egg-code does not give more detailed information such as where exactly the grey ice and the first-year medium ice are located within each segment. Thus, different sea-ice types present in the dataset in a smaller scale (within each segment) were analyzed from the theoretical aspect as an alternative approach.

SAR backscatter in sea-ice imagery depends on the surface roughness and the dielectric constant of sea-ice or open seawater (Deng & Clausi, 2005). The dielectric constant of sea-ice decreases as the degree of salinity decreases. If there is a lower dielectric constant, then the amount of backscattering is high. This implies that the thicker sea-ice will tend to be brighter in color because its salinity is near zero. On the other hand, new or fresh sea-ice tends to be darker in the image since it has a higher dielectric constant, as a result, the amount of backscattering is low. Knowing how various sea-ice types appear in the SAR imagery and with additional knowledge obtained from investigating the egg-codes, the number of different sea-ice types can be carefully determined. Figure 4.5 shows a subset taken from a concentrated sea-ice region.

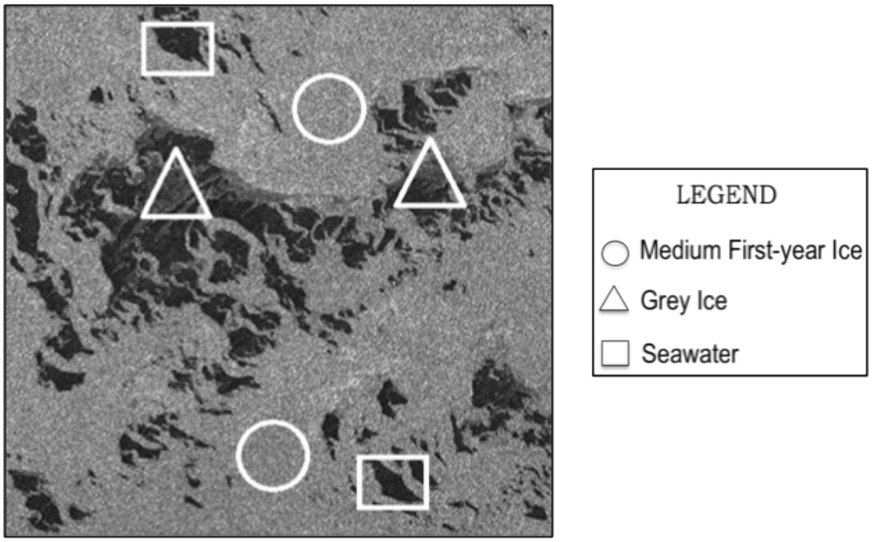

Figure 4.5 Subset taken from the sea-ice region.

As shown in Figure 4.5, three main classes can be extracted from the subset of the image: the circles indicate the relatively thicker ice, possibly being medium first-year ice with a thickness of 70-120 cm (observed higher backscatter return); the triangles indicate the fresh/thin ice, possibly being grey ice with a thickness of 10-15 cm (observed lower backscatter return); and the rectangles identify the seawater (observed very low or no backscatter return). It is important to emphasize that three distinctive classes have been categorized by means of visual inspection with the aid of prior knowledge including varying surface feature characteristics to SAR signals and analysis of egg-codes as discussed previously to help make the right decision. However, the authors want to point out that such analysis can be different from reality. For example, the regions in rectangles could possibly be covered with very thin ice that appears to be equally dark as the seawater. In order to determine whether the detected feature is purely seawater or a very thin ice-covered region, sample intensity values of the seawater were collected from the other part of the same image and compared with the intensity values extracted from the regions in rectangles, where their intensity values were found to be similar, hence it was concluded that the detected feature was seawater. Unless there is additional data revealing what regions were actually present at the time of the image acquisition, analysis has to be done using both the underlying signal difference characteristics of various sea-ice types and seawater, and prior knowledge from examining the ice chart containing egg-codes. To support this method, even trained sea-ice experts at CIS relies on visual inspection and backscattered values as was done in this project. Thus making reliable assumptions based on visual inspection and other conceptual based knowledge is regarded as very important in sea-ice analysis.

4.3.1 Experiment I using Synthetic Data under Noise

In this study, the performance of ETVOS under various noise levels was investigated using synthetic data. A synthetic sea-ice image was created for this experiment, consisting of two different gray levels representing seawater and sea-ice, as shown in Figure 4.6.

Figure 4.6 Synthetic sea-ice image.

To validate the effectiveness and the robustness of the proposed algorithm under noise, multiplicative speckle noise at 11 different noise levels have been applied, ranging between $\sigma^2 = 0.01$ and $\sigma^2 = 0.50$ (increase at an increment of 0.05). The methods used to compare with the proposed ETVOS include the widely used global segmentation methods that are based on the K-means clustering (Redmund et al., 1998) and Gaussian mixture model (Alf et al., 2008). In addition to these two methods, we also applied one additional segmentation scheme. According to (Marques et al., 2004) the segmentation performance can be improved significantly when applying a speckle filter such as Lee, Kuan and Frost filters followed by K-means clustering. These speckle filters have been well recognized for their effectiveness and robustness, as a result they are currently available in many remote sensing software packages. As such, the Frost's adaptive filter was utilized to first eliminate speckle noise and then K-means clustering was used to segment each class in SAR sea-ice imagery. In addition, to show how much improvement the extended ROFTV model containing three penalty terms could make in comparison with the original ROFTV model containing only one penalty term, we included another method. This method replaced the total variation optimization phase of the proposed ETVOS method with the unmodified original ROFTV model and performed the finite mixture classification phase as suggested in the proposed method. This method, using the original ROFTV model followed by the application of 2nd phase of the proposed ETVOS method, is named ROFTV method in this paper.

The test images carried artificial speckles with variances of 0.01, 0.25 and 0.50 at low, mid and high noise levels, respectively as shown in Figure 4.7.

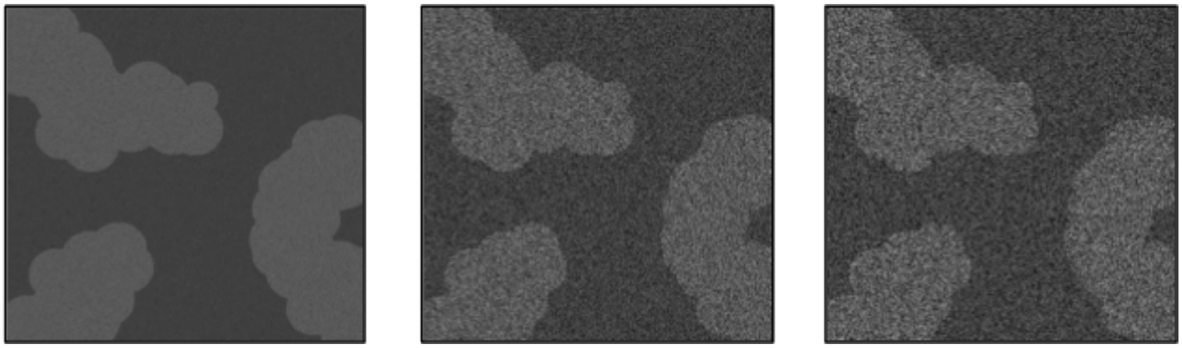

$\sigma^2 = 0.01$ $\sigma^2 = 0.25$ $\sigma^2 = 0.5$

Figure 4.7 Synthetic images used for testing at three different noise levels.

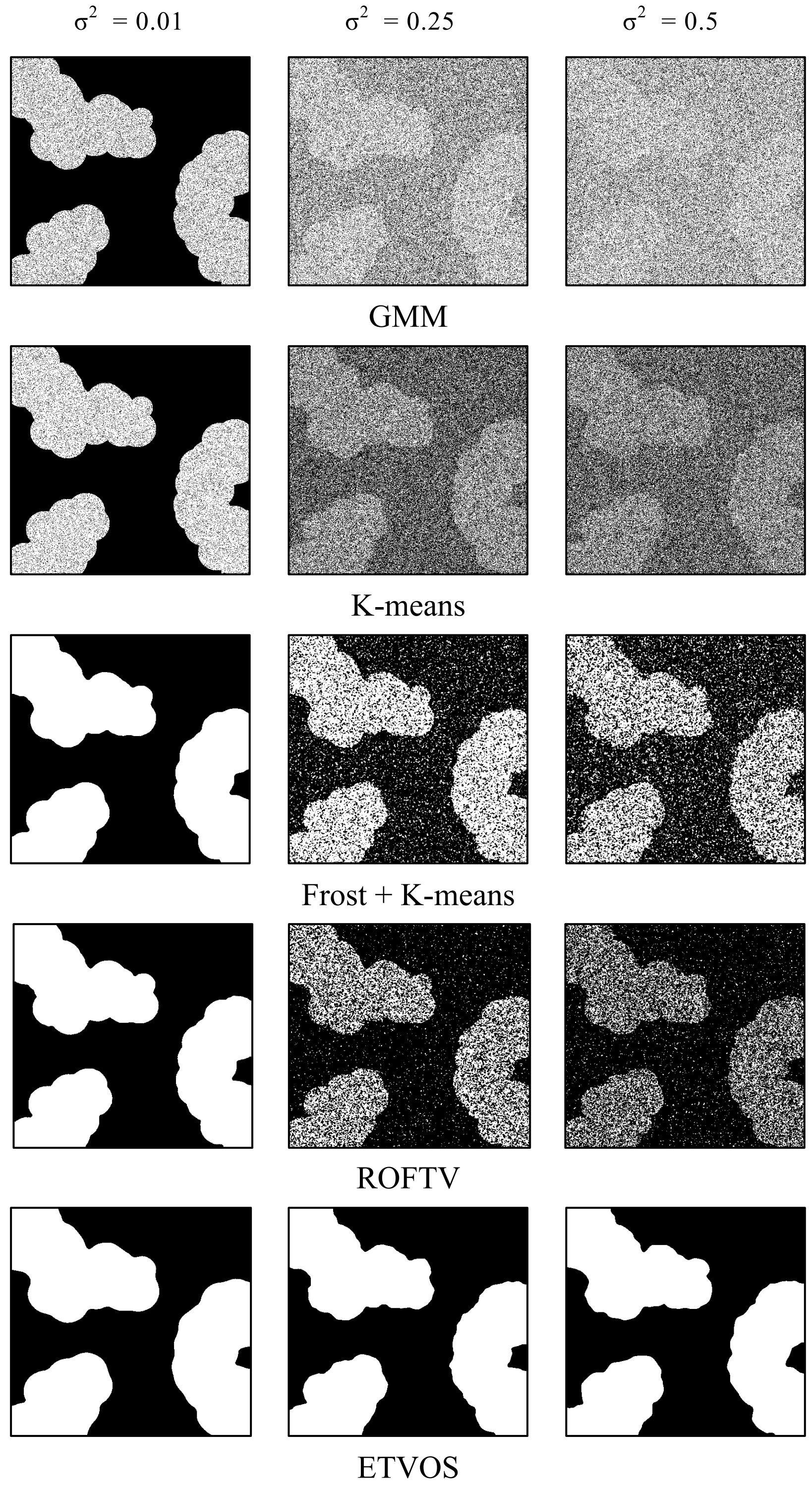

Figure 4.8 Segmentation results on a synthetic image at different speckle noise levels using four methods.

Figure 4.8 illustrates the comparisons of segmentation results using four methods including K-means, GMM, Frost + K-means, and ROFTV with the proposed ETVOS method and shows how each method performs under different speckle noise levels.

As shown in Figure 4.8, the proposed ETVOS method outperforms the rest of four other methods. As the severity of speckle noise embedded in the synthetic image increases, it is well observed that the rest of methods fails to segment two distinct classes. Also note that GMM and K-means segmentation methods fail to an extreme extent. This is mainly due to their segmentation schemes that only take a global tonal characteristic into account making them very weak in removing speckle noises. In addition, the original ROFTV method produced poor segmentation results, leaving many wrongly classified pixels. On the other hand, the segmentation results derived from our proposed method well differentiates two classes. Such satisfactory results are obtained due to the three penalty terms that were incorporated into the extended ROFTV model, with the spatial difference penalty term helping to deal with speckle noise, while the intensity and gradient difference penalty terms help to well preserve boundaries. Hence, the segmentation results using a synthetic test image under different noise levels showed the effectiveness and the robustness of the proposed ETVOS method.

To see these results illustrated in Figure 4.8 in a quantitative fashion, we have performed the F1 score test, which is widely used to validate the accuracy of a test data. It also provides a good measure of how each test method performs under different environments (in our case, different test methods and noise levels). The general formula for F1 score derived based on van Rijsbergen’s effectiveness measure (Van Rijsbergen, 1979) can be expressed by

$$F_1 = \frac{2TP}{2TP + FN + FP}, \tag{4.8}$$

where and TP , FP and FN denote true positive, false positive, and false negative, respectively. By implementing F1 score test, we can observe how accurately the segmentation results are matched with the ground truth image (the original synthetic image) whose F1 score value varies between 0 being absolutely no match and 1 being a perfect match. Figure 4.9 summarizes the F1 scores of five different methods at varying speckle noise levels.

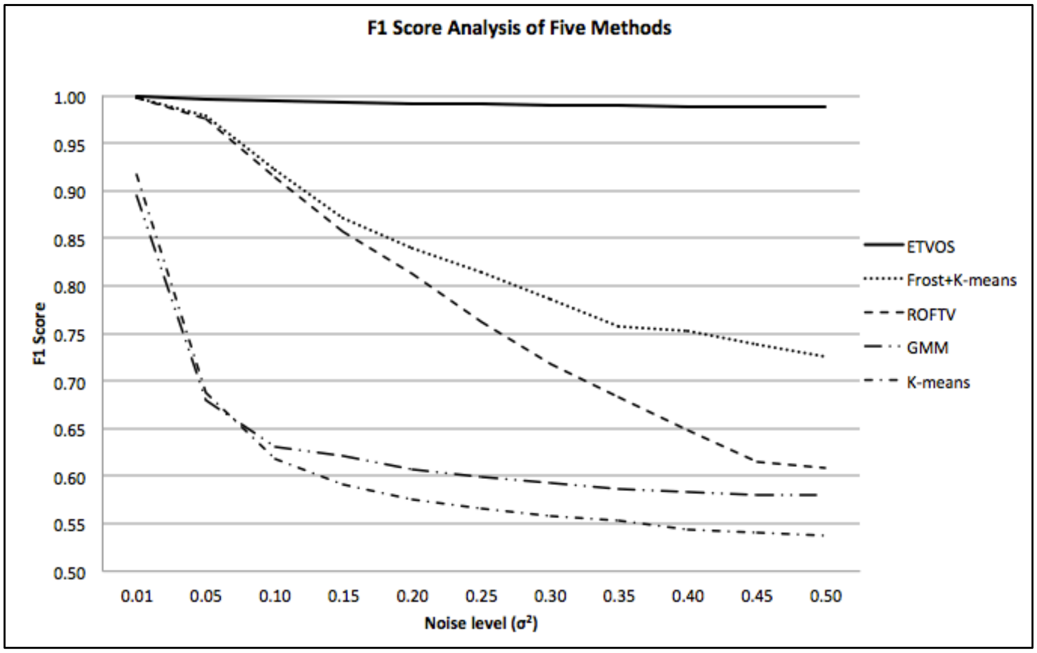

Figure 4.9 F1 score for comparison of five methods at varying noise levels.

It can be observed that the F1 score analysis illustrates the improved segmentation accuracy of the ETVOS method in a quantitative fashion over the other tested segmentation methods. Notice that F1 score of the proposed ETVOS method shows the relatively consistent pattern as shown in flat line whereas F1 score derived from other methods decrease as the amount of embedded noise σ^2 increase. This drop is particularly noticeable for K-means and GMM, as both experienced a dramatic fall between the σ^2 value of 0.01 and 0.05. The Frost + K-means and the ROFTV segmentation method show a relatively better performance than other two since their F1 values did not drop quickly. However, their relatively better segmentation performances grew poorer as the noise levels increased. Through the quantitative validation with respect to its original synthetic image, the proposed ETVOS approach has demonstrated to provide strong segmentation accuracy under high speckle noise.

4.3.2 Experiment II using Real SAR Sea-Ice Imagery

In this section, experimental results from the use of the proposed ETVOS method and four other methods (GMM, K-means, Frost + K-means, and ROFTV) on real SAR sea-ice imagery are presented. Discussion of these methods is followed to indicate which methods produce more promising results. Testing of the proposed method and other methods listed were performed on four test subsets of RADARSAT-2 sea-ice imagery, which are shown in Figure 4.10. The size and the number of classes that were seen from the four test subsets are described in Table 4.1. It is important to note that the number of classes has been determined strictly by visual inspection with underlying knowledge of sea-ice characteristics and egg-code analysis as described earlier.

Table 4-1 Summary of Tested SAR Sea-ice Images

	Size of image (pixels)	Observed number of classes
Test 1	277 x 259	2 (sea-ice and seawater)
Test 2	349 x 340	2 (sea-ice and seawater)
Test 3	384 x 348	3 (grey ice, medium first-year ice, and seawater)
Test 4	505 x 525	3 (grey ice, medium first-year ice, and seawater)

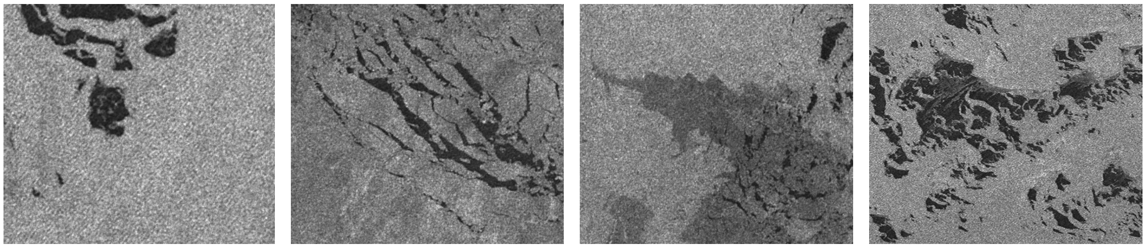
Test 1 Test 2 Test 3 Test 4

Figure 4.10 Subsets of Real RADARSAT-2 SAR sea-ice imagery used for testing.

Figure 4.11 illustrates the segmentation results of the proposed method, ETVOS, and four aforementioned segmentation methods using four test images. The segmentation results produced by GMM, K-means, Frost + K-means, and ROFTV show that while the boundaries of sea-ice areas and seawater are visible, they appear very noisy. The results are particularly noisy for the K-means clustering and GMM segmentation approaches, and is due to the fact that these global segmentation methods only consider global tonal characteristics making them very sensitive to speckle noise while ignoring local spatial relationships. On the other hand, the segmentation results produced by the proposed ETVOS method well preserved the boundaries of seawater and sea-ice. Notice that all of the test images in Figure 4.11 have classified three distinct classes accurately in the results produced using ETVOS. The segmentation results that are derived from the combination of the well-known Frost denoising filter with K-means has proved its effectiveness by Marques et al. who showed that it brings a noticeable improvement when compared to using K-means by itself. However, there still appears to be a large amount of noise in their final products.

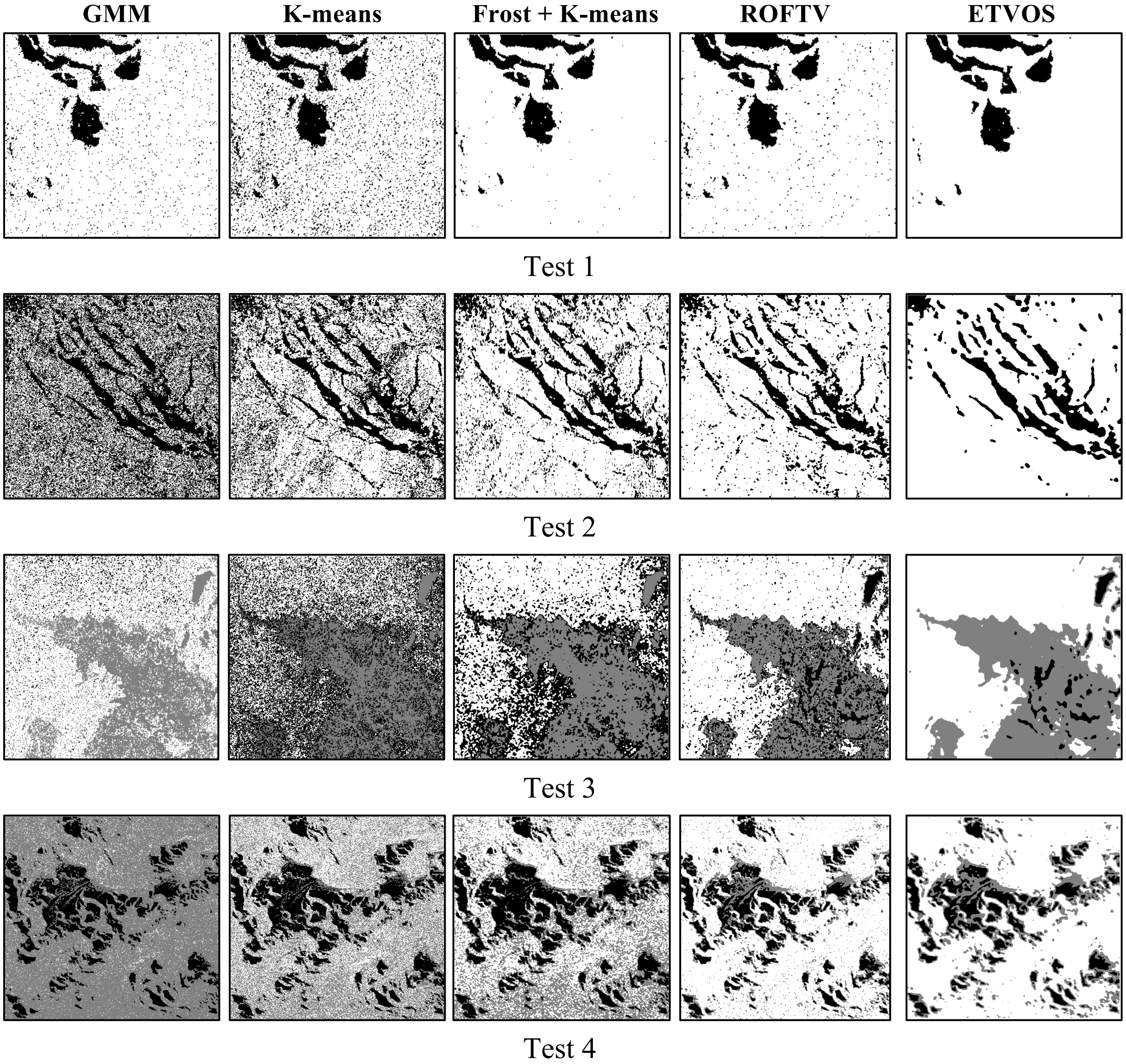

Figure 4.11 Segmentation results on four test sets of real SAR sea-ice imagery using five different methods.

The ROFTV method, which contains only the intensity total variation constraint, produced a relatively better segmentation performance in the real SAR image testing when compared to the others. Such results were obtained due to the data being less noisy, so the utilization of the intensity constraint alone could eliminate noise to a certain extent. However, there still appears to be vast amounts of noise present in the segmented images.

Another notable achievement of the proposed method is that all the results of the ETVOS method form a homogeneity region within each class, whereas other methods produced constant noises within each class. Also, the proposed ETVOS method well supports its possibility to be applied for operational use, as the processing time was short; approximately 8, 12, 16 and 31seconds for test subsets 1, 2, 3 and 4, respectively. The computer used for the testing is equipped with Intel dual core CPUs at 2.4GHz and 3GB of RAM. Therefore it was shown that the proposed ETVOS approach produces superior results compared to other methods.

4.4 Conclusions

This paper introduced a novel SAR sea-ice image segmentation algorithm called enhanced total variation optimization segmentation (ETVOS). This approach first uses an extended total variation optimization phase to construct the piecewise smooth state via three total variation constraints. After the classes in the rough piecewise smooth state has become vividly separable, an expectation maximization approach is then utilized to learn a Gaussian mixture model (GMM). Finally a maximum likelihood classification is performed to assign each pixel into a final class. Based on our experimental results, the proposed method produces a very satisfactory result when compared to other well-established methods. Although a longer processing time is required when incorporating the texture information of sea-ice to the proposed ETVOS method, it can be beneficial in helping to better analyze images with multiple sea-ice types. Thus the study of efficient implementation algorithm combining texture characteristics with the proposed method is highly recommended for future work.

Chapter 5

Conclusions and Recommendations

The research that was undertaken in this thesis was motivated by the essential need to automate the SAR segmentation task and to investigate its feasibility in addressing the environmental issues of Canadian coastal waters. In this last chapter, conclusions that include a summary of the work done and the major achievements are presented in Section 5.1. In Section 5.2, the recommendations for future research are given.

5.1 Conclusions

Canada's marine environment is greatly threatened by deliberate and accidental oil-spills as well as the rapid loss of sea-ice. These phenomena will negatively affect the well-being of humans and threaten the life of many living sea creatures in the Canadian ocean and the Artic. Hence, an effective and efficient way to monitor Canada's coastal waters is essential in order to help minimize the spread of oil-spill pollution, confirm navigable ship routes to ensure safety, and investigate global climate change. The synthetic aperture radar (SAR) onboard Earth observing satellites have been popularly recognized for their profound capability in acquiring data at anytime of the day with a large area coverage. As a result, SAR has become an ideal tool for monitoring the marine environment. However, it is often very laborious, and time-consuming to manually examine thousands of SAR images that are received annually at analysis centres.

Motivated by such challenges, this thesis presents a novel two–phase automated segmentation approach that can accurately detect the desired target being either dark-spots containing possible oil-spills or various different types of sea-ice in a timely manner. Dark-spot detection step in the oil-spill detection process is particularly important as it is considered the most critical step that is required to further proceed to the final classification step where the oil slicks are extracted from look-alikes. The proposed method is named the total variation optimization segmentation (TVOS) approach as it uses multiple constraints to minimize the total variations of the original SAR imagery containing coherent speckle imaging noise, which pose a great difficulty in automatizing the segmentation task.

In the first phase, which is called the total variation optimization phase, two or three total variation penalty terms, depending on the severity of the segmentation task, have been implemented to enforce piecewise smoothness of the original SAR imagery. Total variation minimizers used in this phase include spatial, intensity, and gradient differences to effectively remove the speckles while preserving the boundaries of objects.

In the second phase, which is called the finite mixture classification phase, a purely global classification scheme was utilized. This scheme was implemented since the first-phase processed SAR imagery should contain easily separable classes of dark-spots or non dark-spots, and different types of sea-ice and seawaters. The unknown parameters of the Gaussian mixture model are approximated using an expectation-maximization scheme. When the final class likelihoods are estimated, a maximum likelihood classification technique is utilized to predict the final class of all pixels.

Therefore, the combination of the two aforementioned phases result in a comprehensive segmentation algorithm to efficiently cope with the SAR image segmentation task. In this thesis, an artificially created imagery, which has a similar imaging condition in comparison to real SAR images, was used to test the proposed algorithm. In addition, two real-world SAR images were used to further test the robustness of the proposed algorithm. Segmentation results drawn from other well-established methods were compared to those of the proposed method. The visual inspection of the segmentation results obtained by utilizing the proposed method was observed to provide superior segmentation performance compared to other conventional yet well-established methods.

For synthetic testing, different levels of multiplicative noise, ranging from $\sigma^2 = 0.01$ to 0.70, were applied to an artificially created test imagery whose imaging conditions are very much similar to that of real SAR imagery. In this experiment, the proposed method showed robust segmentation performance even at the highest level of noise, while other methods demonstrated poor segmentation performance. Quantitative data analysis using Cohen's kappa measure (used for dark-spot detection) and the F1 score test (used for sea-ice detection) were employed to validate the segmentation results with the reference data. These two distinct methods provide a good overview of the segmentation result by providing a numerical number, ranging from 1 being a perfect match to 0 being a no-match with respect to the reference data. Kappa and F1 values computed for the proposed method consistently reached near 1 throughout the all noise levels, indicating good matches with the reference data. In contrast, results drawn from other conventional methods showed unpromising segmentation performance since the quantitative measures continually dropped beginning at low to mid noise levels, indicating poor matches with the reference data.

The proposed method was observed to be robust and provided exceptional segmentation performance in the testing of 46 subsets of real COSMO-SkyMed SAR imagery containing verified oil-spills. To perform the dark-spot detection task, only two total variation constraints, including the spatial and the intensity difference terms, were employed considering the relatively less-complex task where only two classes need to be delineated. A visual inspection indicated that the proposed method produced consistent and outstanding results in accurately extracting dark-spots from the background whereas other comparison methods produced unsatisfactory results leaving many wrongly classified pixels. Also the processing time to carry out the segmentation task for the proposed TVOS method was short. For instance, it took only 31 seconds to complete the task using the image with size of 505 x 525 pixels by the proposed method while it took up to 30 minutes to complete a similar task using the mark point process segmentation scheme (Li & Li, 2010).

The proposed method was also tested on various subsets of RADARSAT-2 imagery containing multiple sea-ice types and seawaters. Due to the absence of validation data, the regional ice-chart and egg-codes were used to confirm that the image contained different types of sea-ices. By analyzing the egg-codes of the study area, it was found that it mainly consisted of two ice types; (1) Grey ice with the thickness of 10-15 cm, and (2) Medium first year ice with the thickness of 70 -120 cm. Furthermore, the underlying sea-ice characteristics and their response to SAR signals were examined to provide additional knowledge to correctly identify different sea-ice types and seawaters. Due to the nature of this task being more complex (as there are more classes to identify), three total variation constraints were applied to better handle the segmentation task. The results indicated that the proposed method well delineated the two different types of sea-ice and the seawater in comparison to other tested methods.

In summary, the main contributions of this thesis include: 1) acknowledging the two main on-going issues of oil-spill and sea-ice changes in the Canadian marine environment, 2) studying and understanding the complexity of the feature detection algorithm using a SAR intensity imagery, 3) designing and developing a comprehensive segmentation framework for SAR intensity images, and 4) confirming the superiority of the proposed segmentation framework by visual inspection (for real SAR image testing) and quantitative assessment (for synthetic image testing). As a result, the proposed method was found to be fast, effective, and robust in delivering a satisfactory final segmented result in comparison with other well-established methods.

5.2 Recommendations for Future Research

5.2.1 Incorporation of Additional Total Variation Constraint

The way that the proposed TVOS method was designed makes it easy to adapt another penalty term as an additional constraint to help minimize the total variation of the SAR imagery. Motivated by this, the texture difference term is recommended as an additional constraint to be added to the proposed total variation optimization phase to enhance its ability to further discriminate dark-spots (potential oil-spill) from the background as well as multiple sea-ice types in a more precise fashion. Texture information is considered an important component since SAR imagery contains different characteristics of spatially dependent classes. Different features that appear in images are more likely to have differentiable texture information (Tuceryan & Jain, 1993), thus incorporation of additional texture information will likely enhance the segmentation performance.

5.2.2 Application of PolSAR Imagery

The two real SAR data used in this thesis were acquired in a single polarization mode (VV for oil-spill imagery and HH for sea-ice imagery). With the advent of advanced SAR satellites such as Canadian RADARSAT-2, it has become possible not only to support the selective single polarimetric mode (HH, VV, HV, or VH) but also dual polarimetric mode (HH and HV or VV and VH), and quad polarimetric mode (HH, VV, HV, VH).

In oil-spill detection, the application of dual-polarimetry SAR data is particularly beneficial as it provides three unique physical parameters known as entropy (H), mean scattering angle (α), and anisotropy (A). With these distinctive physical parameters, it becomes much easier to distinguish between look-alikes and actual oil-spills, and moreover it is possible to further analyze the different oil types (Migliaccio et al., 2007).

As for the sea-ice detection, the utilization of the dual-polarimetric data with the combination of different intensity channels will provide the additional information necessary to achieve more accurate estimation of the ice concentrations including the ice thickness (Dierking et al., 2003). Different ice types will have more separations/differences in their backscattered responses, making it easier to define various sea-ice types compared to utilization of single polarimetric data (Dierking et al., 2003).

5.2.3 Utilization of Multi-scale Analysis Technique

SAR images often display very complex patterns and consist of many different local scales that co-exist in the same image, which often form multiple heterogeneous areas. This characteristic has been regarded as a challenge because a single global scale is insufficiently robust in exploiting the information that is essential to correctly interpret the SAR images (Dell'Acqua et al, 2005). Through the course of many experimental tests, it was speculated that the adaptation of a multi-scale processing window used to extract the local pixel information in the first phase of the proposed method would be beneficial to improve the preservation of the detailed feature characteristics. Since the proposed method uses a fixed-size local processing window, it is sometimes hard to process images containing features whose physical sizes are significantly different from each other. Thus, detailed information of relatively small features with respect to the actual size of the image can be preserved by utilizing a processing window of varying scale. However, the challenge of the presence of speckle noise still exists, since images with high speckle noise may not be sufficiently treated when a small local window is used. Thus, it is recommended that the future research should focus on determining the solution to properly incorporate the multi-scale processing window to better preserve the fine details of images and to effectively reduce speckle noise.

References

Achim, A., Tsakalides, P., & Bezerianos, A. (2003). SAR image denoising via Bayesian wavelet shrinkage based on heavy-tailed modeling. *IEEE Trans. Geoscience and Remote Sensing,* 41(8), 1773-1784.

ACIA. (2004). Arctic Climate Impact Assessment. *Impacts of a warming Arctic*. Cambridge: Cambridge University Press.

Alf, M., Nieddu, L., & Vicari, D. (2008). A finite mixture model for image segmentation. *Statistics and Computing*, 18, 137-150.

Alpers, W., & Huehnerfuss, H. (1989). The damping of ocean waves by surface films—a new look at an old problem. *Journal of Geophysical Research*, Vol. 94(C4), 6251-6265.

Aloisio, G., and Cafaro, M. (2003). A dynamic earth observation system. *Parallel Computing*, 29(10), 1357-1362.

Bannerman, K., Caceres, R.G., Rodriguez, M.H., Castillo, O.L., de Miranda, F.P., & Enrico, C. (2009). Operational applications of RADARSAT-2 for the environmental monitoring of oil slicks in the Southern Gulf of Mexico. *International Geoscience and Remote Sensing Symposium*, 3, 381-383.

Barber, D. G. & LeDrew, E. F. (1991). SAR sea-ice discrimination using texture statistics: A multivariate approach. *Photogramm. Eng. Remote Sens*., 57(4), 385-395.

Brekke, C., & Solberg, A. H. S. (2005). Oil spill detection by satellite remote sensing. *Remote Sensing of Environment*, 95(1), 1-13.

Brekke, C., & Solberg, A. H. S. (2008). Classifiers and confidence estimation for oil spill detection in ENVISAT ASAR images. *IEEE Geoscience and Remote Sensing Letters*, 5(1), 65-69.

Brigham, L., & Ellis, B. (2004). *Arctic Marine Transport Workshop*. 28 –30 September 2004, Scott Polar Research Institute, Cambridge University, United Kingdom. 34 p.

Buhasz, L. (2006). Northern underexposure. *Globe & Mail*, July 1.

Canadian Space Agency. (2011). RADARSAT Constellation. [Online]. Available: http://www.asc-csa.gc.ca/eng/satellites/radarsat/default.asp

Chan, T. F., & Vese, L. A., (2001). Active contours without edges. *IEEE Transactions on Image Processing*, 10(2), 266-277.

Chellappa, R. & Chatterjee, S. (1985). Classification of texture using Gaussian Markov random fields. *IEEE Trans. Acoust., Speech, Signal Processing*, ASSP-33, 959-963.

Cheny, M. (2002). Synthetic Aperture Radar. SIAM News, 35(4), 1-2.

Ciappa, A., Pietranera, L., & Coletta, A. (2009). Sea surface transport derived by frequent revisit time series of COSMO SkyMed SAR data. *International Geoscience and Remote Sensing Symposium,* 2, 777-780.

Clausi, D.A. (2001) Comparison and fusion of co-occurrence, Gabor, and MRF texture features for classification of SAR sea-ice imagery, *Atmosphere & Oceans*, 39(4), 183-194.

Clausi, D. A. (2002). An analysis of co-occurrence texture statistics as a function of grey level quantization. *Canadian Journal of Remote Sensing,* 28(1), 1-18.

Intergovernmental Panel on Climate Change (IPCC). (2007). Climate change 2007: IPCC Fourth Assessment Report, *Findings on The Physical Basis of Climate Change*. New York, NY. [Online]. Available: http://www.ipcc.ch/pdf/assessment-report/ar4/syr/ar4_syr.pdf

Cohen, J. (1960). A coefficient of agreement for nominal scales. *Educational and Psychological Measurement*, 20(1), 37–46.

Darbon, J., & Sigelle, M. (2005). Exact optimization of discrete constrained total variation minimization problems. Lecture notes in computer science, 3322, 548-557.

de Miranda, F.P., Marmol, A.M.Q., Pedroso, E.C., Beisl, C.H., Welgan, P., & Morales, L.M. (2004). Analysis of RADARSAT-2 data for offshore monitoring activities in the Cantarell Complex, Gulf of Mexico, using the unsupervised semivariogram textural classifier (USTC). *Canadian Journal of Remote Sensing*, 30(3), 424-436.

Del Frate, F., Petrocchi, A. Lichtenegger, J., & Calabresi, G. (2000). Neural networks for oil spill detection using ERS-SAR data. *IEEE Transactions on Geoscience and Remote Sensing*, 38(5), 2282–2287.

Dell'Acqua, F, Gamba, P., & Trianni, G. (2005). Semi-automatic choice of scale-dependent features for satellite SAR image classification. *Pattern Recognition Letters*, 27, 244-251.

Dempster, A., Laird, N., & Rubin, D. (1977). Maximum likelihood from incomplete data via the EM algorithm. *Journal of the Royal Statistical Society*, Series B, 39(1), 1-38.

Deng, D. & Clausi, D.A. (2005). Unsupervised segmentation of SAR sea-ice imagery using a novel Markov random field model. *IEEE Trans. Geosci. Remote Sensing*, 43(3), 528-538.

de Abreu, R., Gauthier, M., & Wychen, W. V. (2006). SAR-based oil pollution surveillance in Canada: operational implementation and research priorities. *OceanSAR 2006,* 1-4

Dierking, W., Skriver, H., & Gudmandsen, P. (2003). *SAR Polarimetry for Sea-ice Classification*. European Space Agency, (Special Publication), 529, 109-118.

Environment Canada. (2011).

About Canadian Ice Service. [Online].

Available: http://www.ec.gc.ca/glaces-ice/default.asp?lang=En&n=955F6BE5-1

The Egg Code. [Online].

Available: http://www.ec.gc.ca/glaces-ice/default.asp?lang=En&n=84F6AA59-1&wsdoc=FE5C2688-21A8-4165-8FFB-5D28B2A1D943

Daily Sea Ice Chart. [Online].

Available: http://ice-glaces.ec.gc.ca/www_archive/AOI_06/Charts/sc_a06_20090316_WIS27ECT.gif

Eriksson, L.E.B., Berg, A., Borenas, K., Pemberton, P., Lindh, H., Karlson, B., Dierking, W., Santoro, M. (2010). Evaluation of new spaceborne SAR sensors for sea-ice monitoring in the Baltic Sea. *Canadian Journal of Remote Sensing*, 36(1), S56-S73.

Etkin, D. S. (2005). Estimating Cleanup Costs for Oil Spills. *2005 International Oil Spill Conference*, 2625-2634.

Evans, L., & Gariepy, R. (1992). *Measure Theory and Fine Properties of Functions*. CRC Press.

Flett, D., De Abreu, R., Arkett, M., & Gauthier, M.-F. (2008). Initial evaluation of RADARSAT-2 for operational sea-ice monitoring. *IGARSS 2008,* 7-11 July, Boston, MA doi.10.1109/IGARSS.2008.4778779

Ford, J.D., Smit, B., Wandel, J., Allurut, M., Shappa, K., Ittusarjuat, H., & Qrunnut, K. (2008). Climate change in the Arctic: current and future vulnerability in two Inuit communities in Canada. *The Geographical Journal*, 174(1), 45-62.

Frost, V., Stiles, J., Shanmugan, K., & Holtzman, J. (1982). A model for radar images and its application to adaptive digital filtering of multiplicative noise. *IEEE Transactions on Pattern Analysis and Machine Intelligence*, 4(2), 157-166.

Gade, M., & Alpers, W. (1999). Using ERS-2 SAR images for routine observation of marine pollution in European coastal waters. *Science of the Total Environment*. 237-238(1-3), 441-448.

Gens, R. (2008). Oceanographic application of SAR remote sensing. *GIScience & Remote Sensing*, 5(3), 275-305.

Gin, K.Y.H., Huda, MD. K., Lim, W. K., & Tkalich, P. (2001). An Oil Spill-Food Chain Interaction Model for Coastal Waters. *Marine Pollution Bulletin*, 42(7), 590-597.

Girard-Ardhuin, F., Mercier, G., Collard, F., & Garello, R. (2005). Operational oil-slick characterization by SAR imagery and synergistic data. *IEEE Journal of Oceanic Engineering,* 30(3), 487−495.

Grau, M.V. & Groves, T. (1997). The Oil Spill Process: The Effect of Coast Guard Monitoring on Oil Spills. *Environmental and Resource Economics*, 10, 315-339.

Havercamp, D., Soh, L., & Tsatsoulis, C. (1993). A dynamic local thresholding technique for sea-ice classification. *in Proc. IGARSS'93*, 2, 638-640.

Helzel, T., Hansem B., Messtechnik, H. (2010). Remote ocean sensing by HF radar. *International Ocean Systems*, 6-11.

Huebert, R. (2001). Climate change and Canadian sovereignty in the Northwest Passage. *Canadian Journal of Policy Research*, 2(4), 86-94.

Indregard, M., Solberg, A., & Clayton, P. (2005). D2-report on benchmarking oil spill recognition oil spill recognition approaches and best practice. European Commission.

Jha, M., Levy, J., & Gao, Y. (2008). Advances in remote sensing for oil spill disaster management: state-of-the-art sensors technology for oil spill surveillance. *Sensors*, 8(1), 236-255.

Johannessen, O.M., Sandven, S., & Melentyev, V.V. (1997). Icewatch-Ice SAR monitoring of the Northern Sea Route. *6th International Offshore and Polar Engineering Conference*, 2, 417-421.

Karathanassi, V., Topouzelis, K., Pavlakis, P. & Rokos, D. (2006). An object-oriented methodology to detect oil spills. *International Journal of Remote Sensing*, 27(23), 5235-5251.

Karantzalos, K. & Argialas, D. (2008). Automatic detection and tracking of oil spills in SAR imagery with level set segmentation. *International Journal of Remote Sensing.* 29(21), 6281-6296.

Karvonen, J. (2004). Baltic sea ice SAR segmentation and classification using modified pulse-coupled neural networks. *IEEE Trans. Geosci. Remote Sensing*, 42(7), 1566-1574.

Keramitsoglou, I., Cartalis, C., & Kiranoudis, C. (2006). Automatic identification of oil spills on satellite images. *Environmental Modeling & Software*, 21, 640-652.

Khan, K., Yang, J. and Zhang, W. (2007). Unsupervised Classification of Polarimetric SAR Images by EM Algorithm. *IEICE Transactions on Communications*. 90(12), 3632-3642.

Kim, D.J., Moon, W.M., & Kim, Y.S. (2010). Application of TerraSAR-X data for emergent oil-spill monitoring. *IEEE Transactions on Geoscience and Remote Sensing*, 48(2), 852-863.

Kuan, D., Sawchuk, A., Strand, T., & Chavel, P. (1987) Adaptive restoration of images with speckle. *IEEE Transactions on Acoustics, Speech and Signal Process*ing, 35(3), 373-383.

Kubat, M., Holte, R.C., Matwin, S. (1998). Machine Learning for the Detection of Oil Spill in Satellite Radar Images. *Machine Learning*, 30(2-3), 195-215.

Laxon, S., Peacock, N., & Smith, D. (2003). High interannual variability of sea-ice thickness in the Artic region. *Nature*, 425(6961), 947-950.

Lean, G., & Hinrichen, D. (1999). *WWF Atlas of the Environment*. Helicon Publishing.

Lee, J. S. (1980). Digital image enhancement and noise filtering by use of local statistics. *IEEE Transactions on Pattern Analysis and Machine Intelligence*, PAMI-2(2), 165-168.

Lee, J.S, & Jurkevich, I. (1989). Segmentation of SAR Images. *IEEE Transactions on Geoscience and Remote Sensing,* 27(6), 674-680.

Li, Y., & Li, J. (2010). Oil spill detection from SAR intensity imagery using a marked point process. *Remote Sensing of Environment,* 114(7), 1590-1601.

Lira, J. & Frulla, L., (1998). An automated region growing algorithm for segmentation of texture regions in SAR images. *International Journal of Remote Sensing*, 19(18), 3595-3606.

Lu, M., He, Z., & Su, Y. (2009). An active contour model for SAR image segmentation. *IET International Radar Conference*, 551, 1-5.

Marghany, M. (2001). RADARSAT automatic algorithms for detecting coastal oil spill pollution. *International Journal of Applied Earth Observation and Geoinformation*. 3(2), 191-196.

Marques, R.C.P., Carvalho, E.A., Costa, R.C.S., & Medeiros, F.N.S. (2004). Filtering effects on SAR images segmentation, *Lecture Notes in Computer Science*, 3124, 1041-1046.

McCandless, S.W., & Jackson, C.R. (2004). Principles of Synthetic Aperture Radar. In Jackson, C.R., & Apel, J.R. (Eds.), *Synthetic Aperture Radar Marine User's Manual*. (pp. 1-23). Washington, DC: U.S. Department of Commerce.

McLachlan, G. & Krishnan, T. (1997). The EM Algorithm and Extensions. New York: Wiley

Migliaccio, M., Tranfaglia, M., & Ermakov., S. (2005). A physical approach for the observation of oil spills in SAR images. *IEEE Journal of Oceanic Engineering*, 30(3), 496-507.

Migliaccio, M., Gambardella, A., & Tranfaglia, M. (2007). SAR Polarimetry to Observe Oil Spills. *IEEE Transactions on Geoscience and Remote Sensing*, 45(2), 506-511.

Ministry of Environment. (2007). Burnaby Oil Spill [Online]. Available: http://www.env.gov.bc.ca/eemp/incidents/2007/burnaby_oil_spill_07.htm

Ministry of Environment. (2006). M/V Westwood Anette Freighter Oil Spill. [Online]. Available: http://www.env.gov.bc.ca/eemp/incidents/2006/westwood_06.htm

Monaldo, F.M., Thompson, D.R., & Beal, R.C. (2001). Comparison of SAR-derived wind speed with model predictions and ocean buoy measurements. *IEEE Transactions on Geoscience and Remote Sensing*, 39(12), 2587-2600.

National Snow and Ice Data Centre (NSIDC). (2011). State of the Cryosphere. [Online]. Available: http://nsidc.org/sotc/sea_ice.html

Natural Resources Canada. (2005). Canada Centre for Remote Sensing. [Online]. Available: http://www.ccrs.nrcan.gc.ca/glossary/index_e.php?id=2850

Natural Resources Canada. (2011). Sea Ice, The Atlas of Canada. [Online]. Available: http://atlas.nrcan.gc.ca/auth/english/maps/environment/seaice/1

Nirchio, F., Sorgente, M., Giancaspro, A., Biamino, W., Parisato, E., Ravera, R., & Tribero, P. (2005). Automatic detection of oil spills from SAR images. *International Journal of Remote Sensing*, 26(6), 1157-1174.

NOAA, (2007). Emergency Response, Responding to Oil Spills. [Online]. Available: http://response.restoration.noaa.gov/

Nystuen, J. A., & Garcia, F. W. (1992). Sea ice classification using SAR backscatter statistics. *IEEE Trans. Geosci. Remote Sensing,* 30(3), 502-509.

Onstott, R. G. (1992). SAR and Scatterometer Signatures of Sea Ice. In Carsey, F.D. (Eds.), *Microwave Remote sensing of sea ice*. Geophysical Monograph 68, Amer. Geophysical Union, 73-104.

Onstott, R.G., & Shuchman, R.A. (2004). SAR Measurements of Sea Ice. In Jackson, C.R., & Apel, J.R. (Eds.), *Synthetic Aperture Radar Marine User's Manual*. Washington, DC: U.S. Department of Commerce, 81-115.

Otsu, N. (1979). A threshold selection method from gray-level histogram. *IEEE Transactions on Systems, Man and Cybernetics*, 9(1), 62-66.

Park, H., Roberts, G., Aigner, E., Carter, S., Quealy, K., & Xaquin, G.V. (2010). The Oil Spill's Effects on Wildlife. [Online]. Available: http://www.nytimes.com/interactive/2010/04/28/us/20100428-spill-map.html

Pelizzari, S., & Bioucas-Dias, J. (2007). Oil spill segmentation of SAR images via graph cuts, *IGARSS 2007,* 23-28 July, Barcelona, Spain,,1318-1321.Richards, J. A., & Jia, X. (2006). *Remote Sensing Digital Image Analysis*, 4th ed, Berlin, Germany: Springer-Verlag, 67-238.

Piater, J.H. (2002). Mixture Models and Expectation-Maximization. Lecture at ENSIMAG.

Reed, M., Johanse O., Brandvik, P.J., Daling, P., Lewis, A., Fiocco, R., Mackay, D., & Prentki, R. (1999). Oil Spill Modeling towards the Close of the 20th Century: Overview of the State of the Art. *Spill Science & Technology Bulletin,* 5(1), 3-16.

Redmund, Q., Long, D., & Drinkwater, M. (1998). Polar sea-ice classification using enhanced resolution NSCAT data", *in Proc. IGARSS'98*, Seattle, WA, 4, 1976-1978.

Richards, J. A. & Jia, X. 2006. Remote Sensing Digital Image Analysis, 4th ed.; Berlin, Germany: Springer-Verlag, 67-238.

Hasselmann, K., Raney, R. K., Plant, W. J., Alpers, W., Shuchman, R. A., Lyzenga, Rufenach, D. R., C. L., & Tucker, M. J. (1985). Theory of Synthetic Aperture Radar Ocean Imaging: a MARSEN view. *Journal Of Geophysical Research*, 90(C3), 4659-4686.

Rudin, L.I., Ohser, S. & Fatemi, E. (1992). Nonlinear total variation based noise removal algorithms. *Physica D: Nonlinear Phenomena,* 60(1-4), 259-268.

Samadani, R. (1995). A finite mixture algorithm for finding proportions in SAR image. *IEEE Trans. Image Process*ing, 4(8), 1182-1186.

Shi, L., Zhang, X., Seielstad, G., Zhao, C., & He, M. (2007). Oil spill detection by MODIS images using fuzzy cluster and texture feature extraction. *OCEANS 2007 - Europe.* 18-21 June, Aberdeen, UK, 1-5.

Shokr, M. E. (1991). Evaluation of second order texture parameters for sea ice classification from radar images. *J. Geophys. Res.*, 96(C6), 625-640.

Shu, Y., Li, J., Yousif, H., & Gomes, G. (2010). Dark-spot detection from SAR intensity imagery with spatial density thresholding for oil-spill monitoring. *Remote Sensing of Environment*, 114(9), 2026–2035.

Solberg, A. H. S., Storvik, G., Solberg, R., & Volden, E. (1999). Automatic detection of oil spills in ERS SAR images. *IEEE Transactions on Geoscience and Remote Sensing*, 37(4), 1916-1924.

Solberg, A. H. S., Brekke, C., & Husøy, P. O. (2007). Oil spill detection in Radarsat and Envisat SAR Images. *IEEE Transactions on Geoscience and Remote Sensing*, 45(3), 746-755.

Stewart, E.J., Howell, S.E.L., Draper, D. Yackel, J., & Tivy, A. (2007). Sea Ice in Canada's Arctic: Implications for Cruise Tourism. *Artic*, 60(4), 370-380.

Stirling, I., & Parkinson, C.L. (2006). Possible Effects of Climate Warming on Selected Populations of Polar Bears in the Canadian Artic. *Arctic*, 59(3), 261-275.

Suzuki, D. (2011). How tankers and drills threaten Canadian waters. [Online]. Available: http://www.davidsuzuki.org/issues/oceans/science/marine-planning-and-conservation/how-tankers-and-drills-threaten-canadian-waters/

Tian, W., Shao, Y., Yuan, J., Wang, S., & Liu, Y. (2010). An experiment for oil spill recognition using RADARSAT-2 image. *International Geoscience and Remote Sensing Symposium*, 2761-2764.

Tomasi, C. & Manduchi, R. (1998). Bilateral Filtering for Gray and Color Images. *Proceedings of the 1998 IEEE International Conference on Computer Vision,* 839-846.

Topouzelis, K., Karathanassi, V., Pavlakis, P., & Rokos, D. (2008). Dark formation detection using neural networks. *International Journal of Remote Sensing*, 29(16), 4705 – 4720.

Topouzelis, K., Karathanassi, V., Pavlakis, P., & Rokos, D. (2007). Detection and discrimination between oil spills and look-alike phenomena through neural networks. *ISPRS Journal of Photogrammetry and Remote Sensing*, 62(4), 264–270.

Topouzelis, K. N. (2008). Oil spill detection by SAR images: dark formation detection, feature extraction and classification. *Sensors*, 8, 6642-6659.

Transport Canada. (2011). Artic Ship Technology. [Online]. Available: http://www.tc.gc.ca/eng/marinesafety/debs-arctic-construction-standards-tech-1332.htm

Trivero, P., Biamino, W., & Nirchio, F. (2007). High resolution COSMO-SkyMed SAR images for oil spills automatic detection. *IGARSS 2007,* 23-28 July, Barcelona, Spain, 2-5.

Tuceryan, M., and Jain, A. K. (1993). Texture analysis. *Handbook of Pattern Recognition and Computer Vision*, Singapore World Scientific.

Wang, Y., Stoica, P., Li, J., and Marzetta T. (2005). Nonparametric spectral analysis with missing data via the EM algorithm. *Digital Signal Processing*, 15(2), 191-206.

Wolff, C. (2011). Synthetic Aperture Radar. [Online]. Available: http://www.radartutorial.eu/20.airborne/ab07.en.html

Wong, A., Clausi, D. A. & Feiguth, P. (2009). SEC: Stochastic ensemble consensus approach to unsupervised SAR sea-ice segmentation. *2009 Canadian Conference on Computer and Robot Vision*, 299-305.

Yu, Q. & Clausi, D. A. (2007). SAR sea-ice image analysis based on iterative region growing using semantics, *IEEE Trans. Geosci. Remote Sensing,* 45(12), 3919-3931.

Yu. Q., & Clausi, D.A. (2008). IRGS: Image Segmentation Using Edge Penalties and Region Growing. *IEEE Transactions on Pattern Analysis and Machine Intelligence*, 30(12). 2126-2139.

Yu, Y. & Acton, S. (2002). Speckle reducing anisotropic diffusion. *IEEE Trans. Image Process*., 11(11), 1260-1270.

Vachon, P.W., Adlakha, P., Edel, H., Henschel, M., Ramsay, B., Flett, D., Rey, M., Staples, G., & Thomas, S. (2000). Canadian progress toward marine and coastal applications of synthetic aperture radar. *Johns Hopkins Apl Technical Digest*, 21(1), 33-40.

Van Rijsbergen, C. J. (1979). *Information Retrieval* (2nd ed.). MA, USA: Butterworth-Heinemann.

Velotto, D., Lehner, S., & Migliaccio, M. (2010). North Sea Offshore Platform Oil Monitoring by Single and Dual Polarization TerraSAR-X Data. [Online]. Available: http://ieee.uniparthenope.it/chapter/_private/proc10/1.pdf

Zatyagalova, V.V., Ivanov, A.Y., & Golubov, B.N. (2007). Application of Envisat SAR imagery for mapping and estimation of natural oil seeps in the South Caspian Sea. *European Space Agency*, SP-636.